COMPRESSIBILITY EFFECTS ON THE NON-LINEAR RECEPTIVITY OF BOUNDARY LAYERS TO DIELECTRIC BARRIER DISCHARGES

by

MARIE F.C. DENISON

Presented to the Faculty of the Graduate School of
The University of Texas at Arlington in Partial Fulfillment
of the Requirements
for the Degree of

MASTER OF SCIENCE IN AEROSPACE ENGINEERING

THE UNIVERSITY OF TEXAS AT ARLINGTON

May 2013

to Hannes

ACKNOWLEDGEMENTS

I express my sincere gratitude to my supervising professor Dr. Luca Massa for his guidance and support throughout this work and for exposing me to multiple facets of gas dynamics and numerical methods. I wish to thank my academic advisor and committee member Dr. Donald Wilson, for shaping my graduate program and for kindly handling all related questions, and for his interest in my research. I am grateful to Dr. Brian Dennis for his motivating lectures on Computational Fluid Dynamics and for his interest and time reviewing the present work.

I wish to address special thanks to Dr. Ramesh Venugopal, Dr. Borna Obradovic and Lou Hutter my former technology director at Texas Instruments for having been great mentors to me in the past years.

My deepest gratitude goes to my partner Hannes Estl for his loving support and patience during my studies. I am also very grateful to my mother and closest family Françoise, René, Laurence and theirs, as well as to my friends for their precious encouragements.

April 22, 2013

ABSTRACT

COMPRESSIBILITY EFFECTS ON THE NON-LINEAR RECEPTIVITY OF BOUNDARY LAYERS TO DIELECTRIC BARRIER DISCHARGES

Marie F.C. Denison, Ph.D.

The University of Texas at Arlington, 2013

Supervising Professor: Luca Massa

The reduction of drag and aerodynamic heating caused by boundary layer transition is of central interest for the development of hypersonic vehicles. Receptivity to flow perturbation in the form of Tollmien-Schlichting (TS) wave growth often determines the first stage of the transition process, which can be delayed by depositing specific excitations into the boundary layer. Weakly ionized Dielectric Barrier Discharge (DBD) actuators are being investigated as possible sources of such excitations, but little is known today about their interaction with high-speed flows. In this framework, the first part of the thesis is dedicated to a receptivity study of laminar compressible boundary layers over a flat plate by linear stability analysis following an adjoint operator formulation, under DBD representative excitations assumed independent of flow conditions. The second part of the work concentrates on the development of a coupled plasma-Navier and Stokes solver targeted at the study of supersonic flow and compressibility effects on DBD forcing and non-parallel receptivity.

The linear receptivity study of quasi-parallel compressible flows reveals several interesting features such as a significant shift of the region of maximum receptivity

deeper into the flow at high Mach number and strong wave amplitude reduction compared to incompressible flows. The response to DBD relevant excitation distributions and to variations of the base flow conditions and system length scales follows these trends. Observed absolute amplitude changes and relative sensitivity modifications between source types are related to the evolution of the offset between forcing peak profile and relevant adjoint mode maximum. The analysis highlights the crucial importance of designing and placing the actuator in a way that matches its force field to the position of maximum boundary layer receptivity for the specific flow conditions of interest.

In order to address the broad time and length scale spectrum inherent to the compressible flow-plasma problem, a solver has been developed using a novel Adaptive Mesh Refinement (AMR) algorithm based on the *Chombo* design for the solution of partial differential equations. Its embedded boundary formalism is utilized to solve the electro-static potential in the complete domain including the DBD dielectric layer. The program allows accounting for non-equilibrium electron energization and resulting effect on transport and chemical reactions, with air or helium chemistry parametrization. Preliminary direct discharge test cases are reported.

TABLE OF CONTENTS

LIST OF ILLUSTRATIONS

LIST OF TABLES

CHAPTER 1

INTRODUCTION

Plasma-based flow actuation is a growing field of Aerodynamics with prospects to assist control of boundary layers, shock waves, combustion mixing and flame-holding [9–11]. High-energy arc discharges and plasma jets have been demonstrated to significantly affect shock waves and turbulence in boundary layers, engine inlets and compression ramps, through gas heating and momentum transfer optionally assisted by Magneto-Hydrodynamic (MHD) coupling [12,13], but require a significant amount of power. Weakly ionized plasmas in non-thermal equilibrium generated by Dielectric Barrier Discharge (DBD) actuators have shown the ability to influence drag and boundary layer stability, and preliminary studies are being conducted on combustion pre-mixing [14–21]. DBD actuators consist of top and bottom electrodes that are separated by a dielectric material such as Kapton, PVC or Teflon, Fig. 1.1. They are usually operated in glow discharge mode, in which the ion temperature remain close to the background gas temperature whereas electrons are heated up to a few electron-Volts. High differential AC or pulsed voltage in the $1-10kV, 1-10kHz$ range applied between the electrodes causes gas ionization over the exposed side of the dielectric. During each cycle the electron and ion currents transfer momentum and heating to the flow. The maximum velocity transfer to air is estimated below $10-15m/s$ [22,23]. Different force profiles can be realized by using different electrode arrangements [24, 25]. DBD actuators can be flush mounted, they do not include any delicate moving parts and allow depositing excitations into the volume of the boundary layer away from the surface. They can be controlled with response time

down to the order of $\sim \mu s$. As such they are good candidates for implementation as distributed dynamic control surface, that, differently from passive elements, can be activated on-demand without affecting aerodynamic performance in regimes where they are not required.

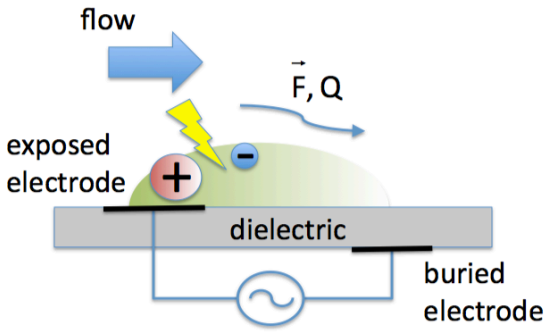

Figure 1.1: Sketch of a DBD actuator.

Plasma patches can modify a boundary layer by introducing optimal perturbations or by changing its receptivity. The first aspect takes advantage of the dispersive property of the base flow, the second aims to modify it. The first approach, i.e., introducing perturbations with an optimal growth rate, requires lower power of actuation. Therefore, it is appropriate for low speed regimes and might even find future application in automobiles [26]. This approach was shown to be effective for amplified fluid systems, e.g., non-separated boundary layers [27]. Some level of influence could be observed on tripping or boundary layer reattachment but more work is needed to determine effectiveness for self-excited systems [28]. The second approach requires significant power at high speed, because its performance depends on the ratio between freestream and actuation velocity. In this case, the power level depends on the structural sensitivity of the boundary region. It can be reduced by determining the region of maximum sensitivity of the base flow and concentrating the excitation therein. This principle is for example applied to the delay of boundary layer tripping

in hypersonic cones and reduction of resulting thermal stress on their shield, by generation of cross-flow perturbations able to suppress the growth of the naturally most amplified mode, using distributed roughness elements [29]. DBD actuators are candidates to generate such forcing [30], but flow receptivity and the dependance of DBD operation on flow conditions and actuator design require further studies. In chapter 2, we will tie to this problem with a linear analysis of the receptivity of two-dimensional quasi-parallel compressible boundary layers over a flat plate, its dependence on flow conditions, and the flow response to excitation profiles representative of DBD actuation under varied scaling.

Because of the complexity of their chemistry and their relative novelty, most DBD actuator studies have been conducted at rest or under flow velocities below 100km/h. Fluid-based discharge models have been developed with few chemical species assuming incompressible flow [31–33], and have been extended to account for photoemission effects and detailed kinetics as for example under nano-second pulsing modeled by means of in-cell particle hybrid computations [34–36]. When applied to high speed flows, the detailed chemistry of weakly ionized plasma discharges, their interactions with shocks and surfaces, transition from glow to filamentary, constricted or bi-modal regime [8, 37], dynamics under fast pulses and actuation mechanisms are still not completely understood, although much progress has been made in the past decade. For example in ref. [38] an MHD model with time dependent compressible Navier-Stokes system was used for inlet boundary layer control by plasma discharge between flush mounted electrodes in a transverse magnetic field, with a plasma model accounting for energy deposition by vibrational excitation of nitrogen and subsequent vibration-translation relaxation. In ref. [39] a three-species (neutral, electron and ion) compressible MHD model was proposed for the study of supersonic inlets controlled by direct plasma discharges. Air plasma models with eight to eleven species con-

sidering non-local energy transport were proposed in ref. [2, 8], and S. Mahadevan investigated in [8] the effects of supersonic flow at Mach 3 on chemistry, convection, cooling and thermalization in direct discharges. It was experimentally shown that supersonic flows can modify the actuator operation mode, with weak shocks and thermal compression in the upstream cathode sheath causing adjacent gas dilatation affecting net momentum transfer [37].

Modeling of such systems requires the resolution of characteristic times stretching from picoseconds at the electron scale to milliseconds at the fluid scale, while the cathode sheath extends over only $100 - 10\mu m$, to compare to the size of an airfoil for instance. Time splitting and parallel computing help handling the resulting stiffness and mesh size [8, 40] but computation remains involved for transient operation of realistic systems such as multi-actuator configurations. With the objective in mind to extend the analysis of chapter 2 to the study of high-speed flow effects on DBD forcing and 3D receptivity analysis, the second part of this work was dedicated to the development of a new plasma-flow solver addressing these challenges. The solver is designed to accommodate flexible chemistry systems and currently implements a three-species helium model after [31] and an eleven-species air model with non-local electron energy treatment from ref. [8], that will be summarized in chapter 3. The program was developed in the C++ *Chombo* platform for the solution of multiscale partial differential equations using block-structured Adaptive Mesh Refinement (AMR), with an embedded boundary formalism allowing to integrate the DBD dielectric layer into the solution domain. The numerical approach will be presented in Chapter 4. Preliminary direct discharges simulations using the helium model will be reported in Chapter 5. Chapter 6 summarizes the results of this work and provides an outline of future research plans.

CHAPTER 2

RECEPTIVITY ANALYSIS

Weak discharges transfer energy into the boundary layer and their main contribution to the development of the instability is the excitation of Tollmien-Schlichting waves. The fraction of the energy released by the DBD that is transferred into the TS wave is denoted as receptivity coefficient and defines the sensitivity of the boundary layer to the related forcing. In this chapter we consider receptivity of quasi-parallel flows to DBD discharges, modeled as separate or combined momentum and heat sources. The analysis centers around the assumption of a spatially developing boundary layer forced at the actuator frequency. This set-up leads to reducing the excitation problem to a pure boundary value problem in the perturbation.

Starting from the linearized compressible Navier-Stokes equation system, the adjoint operator and corresponding eigenvalue systems are derived for the receptivity problem. Their solution obtained by a Chebyshev-τ method are used to analyze compressible flow response to various excitation frequencies, Mach numbers and Reynolds numbers. As a first step, point sources are assumed. Next, forcing is applied in the form of two-dimensional analytical source models of DBD actuators reported in the literature, and receptivity is studied as a function of problem scaling and flow conditions.

2.1 Linearized Navier-Stokes system

The Navier-Stokes compressible system reads

$$\frac{\partial \tilde{\rho}}{\partial t} + \frac{\partial}{\partial x_k}(\tilde{\rho}\tilde{u}_k) = \tilde{s}_{\tilde{\rho}} \tag{2.1a}$$

$$\frac{\partial}{\partial t}(\tilde{\rho}\tilde{u}_i) + \frac{\partial}{\partial x_k}(\tilde{\rho}\tilde{u}_k\tilde{u}_i + \tilde{p}\delta_{ki}) = \frac{\partial \tilde{\tau}_{ki}}{\partial x_k} + \tilde{s}_{\tilde{u}_i} \tag{2.1b}$$

$$\frac{\partial}{\partial t}(\tilde{\rho}\tilde{E}) + \frac{\partial}{\partial x_k}(\tilde{u}_k(\tilde{p} + \tilde{\rho}\tilde{E})) = -\frac{\partial \tilde{q}_{ki}}{\partial x_k} + \frac{\partial}{\partial x_k}(\tilde{\tau}_{ki}\tilde{u}_i) + \tilde{s}_{\tilde{E}} \tag{2.1c}$$

The tilded non-dimensional variables are defined as a function of the problem length-scale L^*, freestream velocity U_∞, temperature T_∞, pressure p_∞, density ρ_∞, dynamic viscosity μ_∞ and thermal conductivity k_∞,

$$\begin{gathered}
\tilde{x} = \frac{x^*}{L^*}, \tilde{y} = \frac{y^*}{L^*}, \tilde{u} = \frac{u^*}{U^*_\infty}, \tilde{v} = \frac{v^*}{U^*_\infty}, \tilde{\rho} = \frac{\rho^*}{\rho^*_\infty}, \tilde{T} = \frac{T^*}{T^*_\infty}, \tilde{E} = \frac{E^*}{U^{*2}_\infty}, \\
\tilde{p} = \frac{p^*}{\rho^*_\infty U^{*2}_\infty}, \tilde{\mu} = \frac{\mu^*}{\mu^*_\infty}, \tilde{k} = \frac{k^*}{k^*_\infty}, \tilde{t} = \frac{t^* U^*_\infty}{L^*}, \tilde{\omega} = \frac{\omega^* L^*}{U^*_\infty}, \\
\mathrm{Re} = \frac{\rho_\infty U_\infty L_\infty}{\mu_\infty}, F \equiv \frac{\omega}{\mathrm{Re}} = 2\pi \frac{f^* \mu^*_\infty}{\rho^*_\infty U^{*2}_\infty}, L^* = \sqrt{\frac{\mu^* x^*}{\rho^*_\infty U^*_\infty}}
\end{gathered} \tag{2.2}$$

where L^* is an estimate of the local boundary layer thickness [1]. The energy, pressure, heat flux and viscous tensor are given by

$$\tilde{E} = \tilde{e} + \frac{1}{2}\tilde{u}_k\tilde{u}_k = \frac{\tilde{T}}{\gamma(\gamma-1)M^2} + \frac{1}{2}\tilde{u}_k\tilde{u}_k \tag{2.3a}$$

$$\tilde{p} = \frac{\tilde{\rho}\tilde{T}}{\gamma M^2} \tag{2.3b}$$

$$\tilde{q_k} = -\frac{\tilde{\mu}}{Pr\mathrm{Re}(\gamma-1)M^2}\frac{\partial \tilde{T}}{\partial x_k} \tag{2.3c}$$

$$\mathrm{Re}\tilde{\tau}_{ki} = \tilde{\mu}\left(\frac{\partial \tilde{u}_i}{\partial x_k} + \frac{\partial \tilde{u}_k}{\partial x_i}\right) + \tilde{\lambda}\frac{\partial \tilde{u}_j}{\partial x_j}\delta_{ik} \tag{2.3d}$$

In these expressions γ is the ratio of the constant pressure and constant volume specific heats $\gamma = c_p/c_v$ and M is the Mach number. The density, momentum and energy

[1] L^* is about one fifth of the Blasius boundary layer. Alternatively, the momentum thickness could be used.

source terms $\tilde{s}_{\tilde{\rho}}$, $\tilde{s}_{\tilde{u}_i}$ and $\tilde{s}_{\tilde{E}}$ account for external excitations for example originating from chemical reactions, acceleration of charged species and heating in an electric field or particle momentum and energy transfers in collision processes. Using these relationships, the energy equation in (2.1) can be expressed in terms of the temperature as follows

$$\frac{\partial \tilde{T}}{\partial t} + \tilde{u}_k \frac{\partial \tilde{T}}{\partial x_k} + \gamma(\gamma-1)M^2 \frac{\tilde{p}}{\tilde{\rho}} \frac{\partial \tilde{u}_k}{\partial x_k} = \frac{\gamma(\gamma-1)M^2}{\tilde{\rho}} \left(\tilde{s}_{\tilde{T}} - \frac{\partial \tilde{q}_k}{\partial x_k} + \tilde{\tau}_{ki} \frac{\partial \tilde{u}_i}{\partial x_k} \right) \tag{2.4}$$

Assuming that each variable can be approximated by the sum of a steady state solution q_s and a small perturbation q, or $\tilde{q} = q_s + q$, the linearized system in the perturbed variables reads

$$\frac{\partial \rho}{\partial t} + u_k \frac{\partial \rho_s}{\partial x_k} + \rho_s \frac{\partial u_k}{\partial x_k} + u_{sk} \frac{\partial \rho}{\partial x_k} + \rho \frac{\partial u_{sk}}{\partial x_k} = s_\rho \tag{2.5a}$$

$$\frac{\partial u_i}{\partial t} + u_{sk} \frac{\partial u_i}{\partial x_k} + \left(u_k + \frac{\rho}{\rho_s} u_{sk} \right) \frac{\partial u_{si}}{\partial x_k} + \frac{1}{\rho_s} \frac{\partial p}{\partial x_i} = s_{u_i} + \frac{1}{\rho_s} \frac{\partial \tau_{ki}}{\partial x_k} \tag{2.5b}$$

$$\begin{aligned} \frac{\partial T}{\partial t} + u_{sk} \frac{\partial T}{\partial x_k} + \left(u_k + \frac{\rho}{\rho_s} u_{sk} \right) \frac{\partial T_s}{\partial x_k} + \frac{\gamma(\gamma-1)M^2}{\rho_s} \left(p_s \frac{\partial u_k}{\partial x_k} + p \frac{\partial u_{sk}}{\partial x_k} \right) = \\ \frac{\gamma(\gamma-1)M^2}{\rho_s} \left(s_T - \frac{\partial q_k}{\partial x_k} + \Phi \right) \end{aligned} \tag{2.5c}$$

with

$$\frac{\partial p}{\partial x_k} = \frac{1}{\gamma M^2} \left(T \frac{\partial \rho_s}{\partial x_k} + \rho_s \frac{\partial T}{\partial x_k} + \rho \frac{\partial T_s}{\partial x_k} + T_s \frac{\partial \rho}{\partial x_k} \right) \tag{2.6a}$$

$$\frac{\partial q_k}{\partial x_k} = -\frac{1}{\mathrm{PrRe}(\gamma-1)M^2} \left(\frac{\partial \mu_s}{\partial x_k} \frac{\partial T}{\partial x_k} + \mu_s \frac{\partial^2 T}{\partial {x_k}^2} + \frac{\partial \mu}{\partial T} \frac{\partial T}{\partial x_k} \frac{\partial T_s}{\partial x_k} + \mu \frac{\partial^2 T_s}{\partial {x_k}^2} \right) \tag{2.6b}$$

$$\begin{aligned} \mathrm{Re}\Phi = 2\mu_s \frac{\partial u_{si}}{\partial x_k} \left(\frac{\partial u_i}{\partial x_k} + \frac{\partial u_k}{\partial x_i} \right) + \frac{\partial \mu}{\partial T} T \frac{\partial u_{si}}{\partial x_k} \left(\frac{\partial u_{si}}{\partial x_k} + \frac{\partial u_{sk}}{\partial x_i} \right) + \\ 2\lambda_s \frac{\partial u_j}{\partial x_j} \frac{\partial u_{sk}}{\partial x_k} + \frac{\partial \lambda}{\partial T} T \left(\frac{\partial u_{sk}}{\partial x_k} \right)^2 \end{aligned} \tag{2.6c}$$

where Φ represents the irreversible linear energy dissipation. In the approximation of a quasi-parallel flow, further simplification can be obtained with

$$q_{s1} = q_s, \; q_{s2} = 0, \; \frac{\partial q_{sk}}{\partial x_1} = 0 \tag{2.7}$$

where like earlier indice s indicates a steady variable. Indice 1 stands for the x-direction of the base flow and indice 2 is the y-direction perpendicular thereto. Using the notations $u_1 = u$ and $u_2 = v$, the linearized system becomes

$$\frac{\partial \rho}{\partial t} + u_s \frac{\partial \rho}{\partial x} + \rho_s \frac{\partial u}{\partial x} + v \frac{\partial \rho_s}{\partial y} + \rho_s \frac{\partial v}{\partial y} = s_\rho \tag{2.8a}$$

$$\begin{aligned}
&\frac{\partial u}{\partial t} + \frac{T_s}{\gamma M^2 \rho_s} \frac{\partial \rho}{\partial x} + \left[u_s \frac{\partial}{\partial x} - \frac{1}{\rho_s \mathrm{Re}} \left((2\mu_s + \lambda_s) \frac{\partial^2}{\partial x^2} + \frac{\partial \mu_s}{\partial y} \frac{\partial}{\partial y} + \mu_s \frac{\partial^2}{\partial y^2} \right) \right] u + \\
&\qquad \left[\frac{\partial u_s}{\partial y} - \frac{1}{\rho_s \mathrm{Re}} \left(\lambda_s \frac{\partial^2}{\partial x \partial y} + \frac{\partial \mu_s}{\partial y} \frac{\partial}{\partial x} + \frac{\partial^2}{\partial x \partial y} \right) \right] v + \\
&\qquad \left[\frac{1}{\gamma M^2} \frac{\partial}{\partial x} - \frac{1}{\rho_s \mathrm{Re}} \left(\frac{\partial \mu}{\partial T} \frac{\partial u_s}{\partial y} \frac{\partial}{\partial y} + \frac{\partial \mu}{\partial T} \frac{\partial^2 u_s}{\partial y^2} + \frac{\partial u_s}{\partial y} \frac{\partial^2 \mu}{\partial T^2} \frac{\partial T_s}{\partial y} \right) \right] T = s_u
\end{aligned} \tag{2.8b}$$

$$\begin{aligned}
&\frac{\partial v}{\partial t} + \frac{1}{\rho_s \gamma M^2} \left[\frac{\partial T_s}{\partial y} + T_s \frac{\partial}{\partial y} \right] \rho - \frac{1}{\rho_s \mathrm{Re}} \left[(\mu_s + \lambda_s) \frac{\partial^2}{\partial x \partial y} + \frac{\partial \lambda_s}{\partial y} \frac{\partial}{\partial x} \right] u + \\
&\qquad \left[u_s \frac{\partial}{\partial x} - \frac{1}{\rho_s \mathrm{Re}} \left(\mu_s \frac{\partial^2}{\partial x^2} + \frac{\partial}{\partial y} (2\mu_s + \lambda_s) \frac{\partial}{\partial y} + (2\mu_s + \lambda_s) \frac{\partial^2}{\partial y^2} \right) \right] v + \\
&\qquad \left[\frac{1}{\rho_s \gamma M^2} \left(\frac{\partial \rho_s}{\partial y} + \rho_s \frac{\partial}{\partial y} \right) - \frac{1}{\rho_s \mathrm{Re}} \left(\frac{\partial u_s}{\partial y} \frac{\partial \mu}{\partial T} \frac{\partial}{\partial x} \right) \right] T = s_v
\end{aligned} \tag{2.8c}$$

$$\begin{aligned}
&\frac{\partial T}{\partial t} + \left[(\gamma - 1) T_s \frac{\partial}{\partial x} - \frac{\gamma(\gamma - 1) M^2}{\rho_s \mathrm{Re}} 2\mu_s \frac{\partial u_s}{\partial y} \frac{\partial}{\partial y} \right] u + \\
&\qquad \left[\frac{\partial T_s}{\partial y} + (\gamma - 1) T_s \frac{\partial}{\partial y} - \frac{\gamma(\gamma - 1) M^2}{\rho_s \mathrm{Re}} 2\mu_s \frac{\partial u_s}{\partial y} \frac{\partial}{\partial x} \right] v + \\
&\qquad \left[u_s \frac{\partial}{\partial x} - \frac{\gamma(\gamma - 1) M^2}{\rho_s \mathrm{Re}} \left(\frac{\partial u_s}{\partial y} \right)^2 \frac{\partial \mu}{\partial T} \right] T - \frac{\gamma}{\rho_s \mathrm{RePr}} \\
&\left[\mu_s \frac{\partial^2}{\partial x^2} + \frac{\partial \mu_s}{\partial y} \frac{\partial}{\partial y} + \mu_s \frac{\partial^2}{\partial y^2} + \frac{\partial T_s}{\partial y} \frac{\partial \mu}{\partial T} \frac{\partial}{\partial y} + \frac{\partial^2 T_s}{\partial y^2} \frac{\partial \mu}{\partial T} + \frac{\partial^2 \mu}{\partial T^2} \left(\frac{\partial T_s}{\partial y} \right)^2 \right] T = s_T
\end{aligned} \tag{2.8d}$$

with reduced components

$$\frac{\partial p}{\partial x} = \frac{1}{\gamma M^2} \left(\rho_s \frac{\partial T}{\partial x} + T_s \frac{\partial \rho}{\partial x} \right) \tag{2.9a}$$

$$\frac{\partial p}{\partial y} = \frac{1}{\gamma M^2} \left(T \frac{\partial \rho_s}{\partial y} + \rho_s \frac{\partial T}{\partial y} + \rho \frac{\partial T_s}{\partial y} + T_s \frac{\partial \rho}{\partial y} \right) \tag{2.9b}$$

$$\frac{\partial q_k}{\partial x_k} = -\frac{\mu}{\mathrm{PrRe}(\gamma - 1) M^2} \left[\mu_s \frac{\partial^2 T}{\partial x^2} + \frac{\partial}{\partial y} \left(\mu_s \frac{\partial T}{\partial y} + \mu \frac{\partial T_s}{\partial y} \right) \right] \tag{2.9c}$$

$$\mathrm{Re}\Phi = 2\mu_s \frac{\partial u_s}{\partial y}\left(\frac{\partial u}{\partial y} + \frac{\partial v}{\partial x}\right) + \mu\left(\frac{\partial u_s}{\partial y}\right)^2 \tag{2.9d}$$

$$\mu = \mu_s + \left.\frac{\partial \mu}{\partial T}\right|_{T_s} T \tag{2.9e}$$

$$\lambda = \lambda_s + \left.\frac{\partial \lambda}{\partial T}\right|_{T_s} T \tag{2.9f}$$

System (2.8) can be summarized in terms of the perturbed variable vector $Q = [u, v, \rho, T]$ and linear operator $\mathcal{L}$ as

$$\frac{\partial Q}{\partial t} + \mathcal{L}(Q) = S \tag{2.10}$$

In the following Q and $\mathcal{L}$ will be referred to as *regular* or *direct* to differentiate them from their adjoint equivalents that are derived in the next section.

2.2 Adjoint operator

Adjoint operators are useful mathematical tools to study the sensitivity of solutions of the linearized Navier-Stokes equations to external forcing [1, 41–43]. The system adjoint operator $\hat{\mathcal{L}}$ can be derived from the Euler-Lagrange identity that itself is obtained from the dot product of a smooth vector field $\hat{\Xi}$ with the linearized Navier-Stokes system

$$Q.\left(\frac{\partial \hat{\Xi}}{\partial t} + \hat{\mathcal{L}}(\hat{\Xi})\right) + \hat{\Xi}.S = \frac{\partial}{\partial t}\Gamma(Q, \hat{\Xi}) + \nabla.J(Q, \hat{\Xi}) \tag{2.11}$$

where Γ is a scalar variable and J is the so-called bilinear concomitant. The adjoint variables $\hat{Q} = \left[\hat{u}, \hat{v}, \hat{\rho}, \hat{T}\right]$ are defined as the solution field satisfying the homogeneous system

$$\frac{\partial \hat{Q}}{\partial t} + \hat{\mathcal{L}}(\hat{Q}) = 0 \tag{2.12}$$

In order to derive $\hat{\mathcal{L}}$, the matrix approach described in [41], Appendix C for an incompressible system is followed, with additional consideration of compressibility

and temperature dependent shear viscosity without bulk counterpart along the lines of M. Baron's treatment of compressible mixing layers in ref. [44]. With this, system (2.8) is formulated as

$$\mathcal{L} = AQ + (B_k Q)_{x_k} + C_k Q_{x_k} + D_{kl} Q_{x_k x_l} \tag{2.13}$$

where the x_k and x_l indices indicate derivation with respect to the related variable (k, l=1,2). Application of the chain rule for differentiation to the dot product with $\hat{Q}$ yields

$$\hat{\mathcal{L}} = (-A^t + C^t_{k,x_k} - D^t_{kl,x_k x_l})\hat{Q} + (B^t_k + C^t_k)\hat{Q}_{x_k} - D^t_{kl}\hat{Q}_{x_k x_l} - D^t_{kl,x_l}\hat{Q}_{x_k} \tag{2.14}$$

which can be expanded as

$$\frac{\partial \hat{\rho}}{\partial t} - u_{sk}\frac{\partial u_{si}}{\partial x_k}\hat{u}_i + u_{sk}\frac{\partial \hat{\rho}}{\partial x_k} + \frac{1}{\gamma M^2}\frac{\partial \hat{u}_k}{\partial x_k} - \left(u_{sk}\frac{\partial T_s}{\partial x_k} + (\gamma-1)T_s\frac{\partial u_{sk}}{\partial x_k}\right)\hat{T} = 0 \tag{2.15a}$$

$$\frac{\partial \hat{u}_i}{\partial t} - \hat{u}_k\frac{\partial u_{sk}}{\partial x_i} + u_{sk}\frac{\partial \hat{u}_i}{\partial x_k} + \frac{\partial \hat{\rho}}{\partial x_i} + \frac{1}{\rho_s}\frac{\partial}{\partial x_i}(\gamma(\gamma-1)M^2 P_s\hat{T}) - \frac{\partial T_s}{\partial x_i}\hat{T} = \frac{1}{\rho_s}\frac{\partial \hat{\tau}_{ik}}{\partial x_k} \tag{2.15b}$$

$$\frac{\partial \hat{T}}{\partial t} + u_{sk}\frac{\partial \hat{T}}{\partial x_k} + \frac{1}{\gamma M^2}\frac{\partial \hat{u}_k}{\partial x_k} - (\gamma-1)\frac{\partial u_{sk}}{\partial x_k}\hat{T} = -\frac{\gamma\mu_s}{\rho_s \mathrm{RePr}}\frac{\partial^2 \hat{T}}{\partial {x_k}^2} + \frac{\hat{\Phi}}{\rho_s} \tag{2.15c}$$

with adjoint viscous tensor, energy dissipation term and adjoint viscosity parameters given by

$$\mathrm{Re}\hat{\tau}_{ik} = 2\gamma(\gamma-1)M^2\mathrm{Re}\tau_{s,ik}\hat{T} - \left(\mu_s\left[\frac{\partial \hat{u}_i}{\partial x_k} + \frac{\partial \hat{u}_k}{\partial x_i}\right] + \lambda_s\frac{\partial \hat{u}_j}{\partial x_j}\delta_{ik}\right) \tag{2.16a}$$

$$\begin{aligned}\mathrm{Re}\hat{\Phi} = &\left[\left.\frac{\partial \mu}{\partial T}\right|_{T_s}\left(\frac{\partial u_{si}}{\partial x_k} + \frac{\partial u_{sk}}{\partial x_i}\right) + \left.\frac{\partial \lambda}{\partial T}\right|_{T_s}\left(\frac{\partial u_k}{\partial x_k}\right)^2\right]\frac{\partial \hat{u}_i}{\partial x_k} - \\ &\frac{\partial u_{si}}{\partial x_k}\left(\frac{\partial u_{si}}{\partial x_k} + \frac{\partial u_{sk}}{\partial x_i}\right)\hat{\mu} - \left(\frac{\partial u_{sk}}{\partial x_k}\right)^2\hat{\lambda} - \frac{\gamma}{\mathrm{Pr}}\left(\frac{\partial \mu_s}{\partial x_k} - \frac{\partial \mu}{\partial T}\frac{\partial T_s}{\partial x_k}\right)\frac{\partial \hat{T}}{\partial x_k}\end{aligned} \tag{2.16b}$$

$$\hat{\mu} = \gamma(\gamma-1)M^2\left.\frac{\partial \mu}{\partial T}\right|_{T_s}\hat{T} \tag{2.16c}$$

$$\hat{\lambda} = \gamma(\gamma-1)M^2\left.\frac{\partial \lambda}{\partial T}\right|_{T_s}\hat{T} \tag{2.16d}$$

The scalar variable Γ and bilinear concommitant J at the RHS of the Euler-Lagrange identity (2.11) read

$$\frac{\partial \Omega}{\partial t} = \frac{\partial}{\partial t}\left(\rho\hat{\rho} + \rho_s(u_k\hat{u_k} + T\hat{T})\right) \tag{2.17a}$$

$$\begin{gathered} J_i = u_{si}(\rho\hat{\rho} + \rho_s(u_k\hat{u}_k + T\hat{T})) + p\hat{u}_i + \hat{p}u_i - \hat{u}_k\tau_{ki} - u_k\hat{\tau}_{ki} + \\ \frac{\gamma}{\mathrm{PrRe}}\left[\mu_s\left(T\frac{\partial \hat{T}}{\partial x_i} - \hat{T}\frac{\partial T}{\partial x_i}\right) - T\hat{T}\frac{\partial \mu_s}{\partial x_i}\right] \end{gathered} \tag{2.17b}$$

$$\hat{p} = \rho_s(\hat{\rho} + (\gamma - 1)T_s\hat{T}) \tag{2.17c}$$

As earlier the system can be simplified in case of a quasi-parallel flow, resulting in

$$\frac{\partial \hat{\rho}}{\partial t} + u_s\frac{\partial \hat{\rho}}{\partial x} + \frac{T_s}{\gamma M^2}\left(\frac{\partial \hat{u}}{\partial x} + \frac{\partial \hat{v}}{\partial y}\right) = 0 \tag{2.18a}$$

$$\frac{\partial \hat{u}}{\partial t} + u_s\frac{\partial \hat{u}}{\partial x} + \frac{\partial \hat{\rho}}{\partial x} + (\gamma - 1)T_s\frac{\partial \hat{T}}{\partial x} = \frac{1}{\rho_s}\left(\frac{\partial \hat{\tau}_{xx}}{\partial x} + \frac{\partial \hat{\tau}_{xy}}{\partial y}\right) \tag{2.18b}$$

$$\begin{gathered} \frac{\partial \hat{v}}{\partial t} - u\frac{\partial \hat{u}_s}{\partial y} + u_s\frac{\partial \hat{v}}{\partial x} + \frac{1}{\rho_s}\frac{\partial \hat{\rho}}{\partial y} + (\gamma - 1)T_s\frac{\partial \hat{T}}{\partial y} \\ + \frac{\gamma(\gamma - 1)M^2}{\rho_s}\frac{\partial p_s}{\partial y} - \frac{\partial T_s}{\partial y}\hat{T} = \frac{1}{\rho_s}\left(\frac{\partial \hat{\tau}_{xy}}{\partial x} + \frac{\partial \hat{\tau}_{yy}}{\partial y}\right) \end{gathered} \tag{2.18c}$$

$$\frac{\partial \hat{T}}{\partial t} + u_s\frac{\partial \hat{T}}{\partial x} + \frac{1}{\gamma M^2}\left(\frac{\partial \hat{u}}{\partial x} + \frac{\partial \hat{v}}{\partial y}\right) = -\frac{\gamma\mu_s}{\rho_s\mathrm{RePr}}\left(\frac{\partial^2 \hat{T}}{\partial x^2} + \frac{\partial^2 \hat{T}}{\partial y^2}\right) + \frac{\hat{\Phi}}{\rho_s} \tag{2.18d}$$

where new adjoint components are defined as

$$\begin{gathered} \frac{\partial \hat{\tau}_{xx}}{\partial x} + \frac{\partial \hat{\tau}_{xy}}{\partial y} = \frac{2\gamma(\gamma - 1)M^2}{\mathrm{Re}}\frac{\partial}{\partial y}\left(\mu_s\frac{\partial u_s}{\partial y}\hat{T}\right) + \\ \frac{1}{\mathrm{Re}}\left(-(2\mu_s + \lambda_s)\frac{\partial^2 \hat{u}}{\partial x^2} - (\mu_s + \lambda_s)\frac{\partial^2 \hat{v}}{\partial x \partial y} - \mu_s\frac{\partial^2 \hat{u}}{\partial y^2} - \frac{\partial \mu_s}{\partial y}\frac{\partial \hat{u}}{\partial y} - \frac{\partial \mu_s}{\partial y}\frac{\partial \hat{v}}{\partial x}\right) \end{gathered} \tag{2.19a}$$

$$\begin{gathered} \frac{\partial \hat{\tau}_{xy}}{\partial x} + \frac{\partial \hat{\tau}_{yy}}{\partial y} = \frac{2\gamma(\gamma - 1)M^2}{\mathrm{Re}}\mu_s\frac{\partial u_s}{\partial y}\frac{\partial \hat{T}}{\partial x} + \\ \frac{1}{\mathrm{Re}}\left(-(2\mu_s + \lambda_s)\frac{\partial^2 \hat{v}}{\partial y^2} - (\mu_s + \lambda_s)\frac{\partial^2 \hat{u}}{\partial x \partial y} - \mu_s\frac{\partial^2 \hat{v}}{\partial x^2} - \frac{\partial \lambda_s}{\partial y}\frac{\partial \hat{u}}{\partial x} - \frac{\partial}{\partial y}(2\mu_s + \lambda_s)\frac{\partial \hat{v}}{\partial y}\right) \end{gathered} \tag{2.19b}$$

$$\mathrm{Re}\hat{\Phi} = \frac{\partial \mu}{\partial T}\frac{\partial u_s}{\partial y}\left(\frac{\partial \hat{v}}{\partial x} + \frac{\partial \hat{u}}{\partial y}\right) - \hat{\mu}\left(\frac{\partial^2 u_s}{\partial y^2}\right)^2 - \frac{\gamma}{\mathrm{Pr}}\left(\frac{\partial \mu_s}{\partial y} - \frac{\partial \mu}{\partial T}\frac{\partial T_s}{\partial y}\right)\frac{\partial \hat{T}}{\partial y} \tag{2.19c}$$

The bilenar concommitant components become

$$J_x = u_s(\rho\hat{\rho} + \rho_s(u\hat{u} + v\hat{v} + T\hat{T})) + p\hat{u} + \hat{p}u - (\hat{u}\tau_{xx} + \hat{v}\tau_{yx} + u\hat{\tau}_{xx} + v\hat{\tau}_{yx}) + \frac{\gamma\mu_s}{\mathrm{PrRe}}\left(T\frac{\partial\hat{T}}{\partial x} - \hat{T}\frac{\partial T}{\partial x}\right) \tag{2.20a}$$

$$J_y = p\hat{v} + \hat{p}v - (\hat{u}\tau_{xy} + \hat{v}\tau_{yy} + u\hat{\tau}_{xy} + v\hat{\tau}_{yy}) + \frac{\gamma}{\mathrm{PrRe}}\left[\mu_s\left(T\frac{\partial\hat{T}}{\partial y} - \hat{T}\frac{\partial T}{\partial y}\right) - \frac{\partial\mu_s}{\partial y}T\hat{T}\right] \tag{2.20b}$$

2.3 Modal solutions

The sensitivity of the response of the boundary layer to an excitation at frequency ω can be studied by treating system (2.8) and (2.18) as boundary value problems in the perturbations Q and $\hat{Q}$

$$-i\omega Q + \mathcal{L}(Q) = S_Q \text{ on } \Omega, \tag{2.21a}$$

$$BQ = S_B \text{ on } \partial\Omega \tag{2.21b}$$

$$i\omega\hat{Q} + \hat{\mathcal{L}}\left(\hat{Q}\right) = 0 \text{ on } \Omega, \tag{2.21c}$$

$$\hat{B}\hat{Q} = 0 \text{ on } \partial\Omega \tag{2.21d}$$

where S_B and S_Q are source term vectors and B, $\hat{B}$ are matrices of boundary coefficients. Assuming a normal mode solution of the form $A_\phi\phi(y,z)\exp(\pm i\alpha x)$, where x is the streamwise direction and where the positive sign relates to the regular variable and the negative sign to the adjoint field, we determine A_ϕ using the Euler-Lagrange identity (2.11). The second order differential operators $\mathcal{L}$, $\hat{\mathcal{L}}$ are formulated as a sum of terms of different y-derivative order where y is perpendicular to the boundary

$$\mathcal{L} \equiv A\frac{\partial^2}{\partial y^2} + B\frac{\partial}{\partial y} + C \tag{2.22a}$$

$$\hat{\mathcal{L}} \equiv \hat{A}\frac{\partial^2}{\partial y^2} + \hat{B}\frac{\partial}{\partial y} + \hat{C} \tag{2.22b}$$

and we decompose the matrices $A, B, C, \hat{A}, \hat{B}$ and $\hat{C}$ into inviscid and viscous components that will be denoted with subscript i and v, respectively. In the following equations the $'$ symbol indicates differentiation with respect to y and the $\dot{(\cdot)}$ indicates differentiation with respect to temperature. The regular matrices due to viscosity read

$$A_v \equiv \frac{1}{\rho \mathrm{Re}} \begin{pmatrix} -\mu & 0 & 0 & 0 \\ 0 & -\frac{4\mu}{3} & 0 & 0 \\ 0 & 0 & 0 & 0 \\ 0 & 0 & 0 & -\zeta \end{pmatrix}, B_v \equiv \frac{1}{\rho \mathrm{Re}} \begin{pmatrix} -\dot{\mu}T' & -\frac{1}{3}i\alpha\mu & 0 & -\dot{\mu}u' \\ -\frac{1}{3}i\alpha\mu & -\frac{4\dot{\mu}T'}{3} & 0 & 0 \\ 0 & 0 & 0 & 0 \\ -2\xi u' & 0 & 0 & -2\dot{\zeta}T' \end{pmatrix},$$

$$C_v \equiv \frac{1}{\rho \mathrm{Re}} \begin{pmatrix} \frac{4\alpha^2\mu}{3} & -i\alpha\dot{\mu}T' & 0 & -\ddot{\mu}T'u' - \dot{\mu}u'' \\ \frac{2}{3}i\alpha\dot{\mu}T' & \alpha^2\mu & 0 & -i\alpha\dot{\mu}u' \\ 0 & 0 & 0 & 0 \\ 0 & -2i\alpha\xi u' & 0 & \zeta\alpha^2 - \ddot{\zeta}T'^2 - \dot{\xi}u'^2 - \dot{\zeta}T'' \end{pmatrix}. \tag{2.23}$$

The corresponding adjoint operators are,

$$\hat{A}_v \equiv \frac{1}{\rho \mathrm{Re}} \begin{pmatrix} \mu & 0 & 0 & 0 \\ 0 & \frac{4\mu}{3} & 0 & 0 \\ 0 & 0 & 0 & 0 \\ 0 & 0 & 0 & \zeta \end{pmatrix}, \hat{B}_v \equiv \frac{1}{\rho \mathrm{Re}} \begin{pmatrix} \mu' & -\frac{1}{3}i\alpha\mu & 0 & -2\xi u' \\ -\frac{1}{3}i\alpha\mu & \frac{4\mu'}{3} & 0 & 0 \\ 0 & 0 & 0 & 0 \\ -\dot{\mu}u' & 0 & 0 & 0 \end{pmatrix},$$

$$\hat{C}_v \equiv \frac{1}{\rho \mathrm{Re}} \begin{pmatrix} -\frac{4\alpha^2\mu}{3} & -i\alpha\mu' & 0 & -2\left(\dot{\xi}T'u' + \xi u''\right) \\ \frac{2i\alpha\mu'}{3} & -\alpha^2\mu & 0 & 2i\alpha\xi u' \\ 0 & 0 & 0 & 0 \\ 0 & i\alpha\dot{\mu}u' & 0 & \dot{\xi}u'^2 - \alpha^2\zeta \end{pmatrix} \tag{2.24}$$

where $\zeta \equiv \gamma\mu/\mathrm{Pr}$ typifies the effect of the thermal conductivity and $\xi \equiv \gamma\left(\gamma-1\right)M^2\mu$. The inviscid part of the linear operators is of the first order in $\frac{\partial}{\partial y}$, thus $A_i = A_i = 0$, and the remaining matrices are

$$B_i \equiv \begin{pmatrix} 0 & 0 & 0 & 0 \\ 0 & 0 & \frac{R_g T}{\rho} & R_g \\ 0 & \rho & 0 & 0 \\ 0 & (\gamma-1)T & 0 & 0 \end{pmatrix}, C_i \equiv \begin{pmatrix} i\alpha u & u' & \frac{i\alpha R_g T}{\rho} & i\alpha R_g \\ 0 & i\alpha u & \frac{R_g T'}{\rho} & -\frac{R_g T'}{T} \\ i\alpha\rho & -\frac{\rho T'}{T} & i\alpha u & 0 \\ i\alpha(\gamma-1)T & T' & 0 & i\alpha u \end{pmatrix} \tag{2.25}$$

$$\hat{B}_i \equiv \begin{pmatrix} 0 & 0 & 0 & 0 \\ 0 & 0 & 1 & (\gamma-1)T \\ 0 & R_g T & 0 & 0 \\ 0 & R_g & 0 & 0 \end{pmatrix}, \hat{C}_i \equiv \begin{pmatrix} -i\alpha u & 0 & -i\alpha & -i\alpha(\gamma-1)T \\ -u' & -i\alpha u & 0 & -T' \\ -i\alpha R_g T & 0 & -i\alpha u & 0 \\ -i\alpha R_g & 0 & 0 & -i\alpha u \end{pmatrix}, \tag{2.26}$$

where R_g is a constant that in the dimensional equations is equal to the specific gas constant, while in the present dimensionless case is $R_g \equiv \frac{1}{\gamma M^2}$. The bilinear concomitant components in (2.20) J_α with $\alpha = x, y$ can be expressed in the form of

$\hat{Q}^t(D_\alpha \frac{\partial}{\partial y})Q + Q^t(-D_\alpha \frac{\partial}{\partial y} + E_\alpha)\hat{Q}$ where the component specific matrices D_x, E_x, D_y and E_y are given by

$$D_x = \begin{pmatrix} 0 & -\frac{\lambda}{\mathrm{Re}} & 0 & 0 \\ -\frac{\mu}{\mathrm{Re}} & 0 & 0 & 0 \\ 0 & 0 & 0 & 0 \\ 0 & 0 & 0 & 0 \end{pmatrix}, D_y = \begin{pmatrix} -\frac{\mu}{\mathrm{Re}} & 0 & 0 & 0 \\ 0 & -\frac{2\mu+\lambda}{\mathrm{Re}} & 0 & 0 \\ 0 & 0 & 0 & 0 \\ 0 & 0 & 0 & -i\alpha\frac{\zeta}{\mathrm{Re}} \end{pmatrix},$$

$$E_x = \begin{pmatrix} u\rho - 2i\alpha\frac{2\mu+\lambda}{\mathrm{Re}} & 0 & R_gT & R_g\rho \\ 0 & u\rho - 2i\alpha\frac{\mu}{\mathrm{Re}} & 0 & -\frac{\dot{\mu}u'}{\mathrm{Re}} \\ \rho & 0 & u & 0 \\ \rho(\gamma-1)T & -\frac{2(\gamma-1)}{\mathrm{Re}R_g}\mu u' & 0 & \rho u - 2i\alpha\frac{\zeta}{\mathrm{Re}} \end{pmatrix}, \tag{2.27}$$

$$E_y = \begin{pmatrix} 0 & -2i\alpha\frac{\mu}{\mathrm{Re}} & 0 & -\frac{\dot{\mu}u'}{\mathrm{Re}} \\ -2i\alpha\frac{\lambda}{\mathrm{Re}} & 0 & R_gT & R_g\rho \\ 0 & \rho & 0 & 0 \\ -\frac{2(\gamma-1)}{\mathrm{Re}Rg}\mu u' & \rho(\gamma-1)T - \frac{2(\gamma-1)}{\mathrm{Re}Rg}\mu u' & 0 & -\frac{\gamma}{\mathrm{RePr}}\mu' \end{pmatrix}.$$

The adjoint property of the above operators and the bilinear concomitant were verified from the Euler-Lagrange identity using harmonic test functions. The adjoint system was also verified in Mathematica by Taylor expansion of the variables and application of the Euler-Lagrange identity under physical parameter contraints and quasi-parallel simplification rules.

When studying a perturbation source of the form $S = s(x, y)\exp(-i\omega t)$ with compact support in the domain $\{a < x < b, y > 0\}$, the far field can be described by the solution to the homogeneous system. Therefore, the amplitude of a mode of given wave number α at coordinate x_b downstream of the source can be found from the Euler-Lagrange identity (2.11) and the bi-orthogonality between adjoint and regular

modes with respect to the inner product $[\phi_m, \hat{\phi}_n] = \int_0^\infty J_x(\phi_m, \hat{\phi}_n)dy = \delta_{mn}$ [1, 41, 42] as

$$A_\phi|_{x=b} = \frac{\int_a^b \int_0^\infty s(x,y)\hat{\phi}(y)\exp(-i\alpha x)\,dxdy}{[\phi, \hat{\phi}]}. \tag{2.28}$$

If the perturbation emanates from or touches the wall, such as in presence of suction/blowing at the surface of the plate, its effect can be accounted for by adding to (2.28) the contribution of the y-component of the bilinear concomitant J_y (for a flat plate),

$$A_\phi|_{x=b} = \frac{\int_a^b \int_0^\infty s(x,y)\hat{\phi}(y)\exp(-i\alpha x)\,dxdy + \int_{x_a}^{x_b} J_y(x,0)dx}{[\phi, \hat{\phi}]}. \tag{2.29}$$

This case will not be considered here, but it is a straightforward extension when required. Thus, the receptivity coefficients can be calculated for any number of forcing conditions using only the solutions of the homogeneous regular and adjoint systems equation (2.21) with $S_Q = 0$, which can be readily calculated and only need to be computed once. The physical interpretation of the adjoint eigenmodes can be highlighted by normalizing the regular modes by the maximum absolute value of the horizontal velocity over the y-domain, and the adjoint modes by $[\phi, \hat{\phi}] = 1$ as described by D. Hill in ref. [1]. With this normalization, and considering a point source $s(x, y) = \Delta(x_0, y_0)$ where Δ denotes the *Dirac* function, equation (2.28) reduces to

$$|A_\phi| = \hat{\phi}(y_0). \tag{2.30}$$

so that the adjoint modes give the amplification factor to a unit point source applied at height y_0, for a unit horizontal perturbed velocity. The flow response to a distributed force is given by equation (2.28) at a given harmonic forcing frequency ω and corresponding unstable wavenumber α. More complex temporal waveforms can be analyzed by Fourier decomposition of the source terms and summation of the components overlapping with the eigenvalue spectrum of the flow.

2.4 Adjoint modal analysis

The eigenmode and eigenvalue solutions to (2.21) were obtained using the Chebyshev $\tau - QZ$ method [41, 45]. Following this spectral method, the dependent variables are expressed as a truncated series of Chebyshev polynomials representing the variations of the dependent variables in the inhomogeneous y-direction. In the τ method a Rayleigh-Ritz procedure is used to project the continuous dependent variables into the space spanned by the polynomials. Recurrence properties relating the derivatives of the Chebyshev polynomials at those points allows formulating the homogeneous part of (2.21) as an eigenvalue systems of which the solutions are the polynomial coefficients in the truncated series representing the variables. In the τ method, additional coefficients are included into the solution system, that are measures of the truncation error, and the differential operators and boundary conditions are treated in a way that minimizes the occurrence of spurious values as for example arising from rows of zeros in the eigenvalue matrix.

Since the domain over the flat plate is semi-infinite and the convective Mach number in the freestream is kept lower than one, only one physical unstable eigenmode can be found for any given ω, Re and M combination. The quadratic eigenvalue system solution yields a number of eigenvalues approximately equal (considering boundary conditions) to the double of the number of Chebyshev polynomials (here typically equal to 130). Spurious eigenvalues are filtered based on the sign of their imaginary part, independence on polynomial count and grid size, as well as identity between regular and adjoint solutions.

Eigenvalues with negative imaginary part (i.e., $\alpha_i \equiv \mathrm{Im}\,(\alpha) < 0$) represent unstable perturbation waves. No unstable eigenvalue is found for non-dimensional frequencies above 0.08 for Mach numbers ranging from 0.5 to 2 and Reynolds number varying between 500 and 5000. The maximum amplitude of the wave number

imaginary component decreases with increasing Mach number and increases with Reynolds number until the calculated value Re = 2000, see Fig. 2.1. Further, Fig. 2.2 and Fig. 2.3 show typical examples of TS modes normalized by the maximum absolute value of the $\hat{u}$ eigenvector and corresponding adjoint modes normalized such that $[\phi\hat{\phi}] = 1$ per previous section, zoomed in the wall region (y_∞ is typically > 250 for $M > 1$). Comparison of these figures shows an increased amplitude of the regular density and temperature fields at $M = 1.5$. Per equations (2.28) and (2.30), a source term of a given type (momentum, heating or density) is expected to have more influence on the receptivity when located in a region around the maximum amplitude of the related variable adjoint eigenmode.

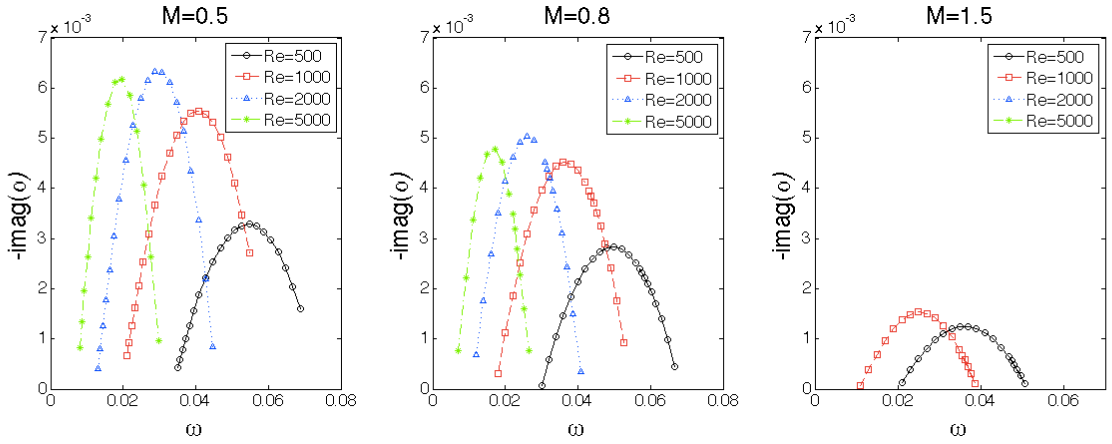

Figure 2.1: Negative imaginary part of the unstable TS mode wave number versus forcing frequency ω, Reynolds number Re and Mach number M.

In this respect Fig. 2.4 reports the position of the maximum of each eigenmode (upper plots) and corresponding maximum amplitude at $M = 0.5$. For all variables, the peak is located in the range of the hydrodynamic length scale in (2.2). For the adjoint horizontal velocity $\hat{u}$ the y-coordinate corresponding to the so-called critical velocity at which the mean flow horizontal velocity is equal to the phase velocity $c_r \equiv$

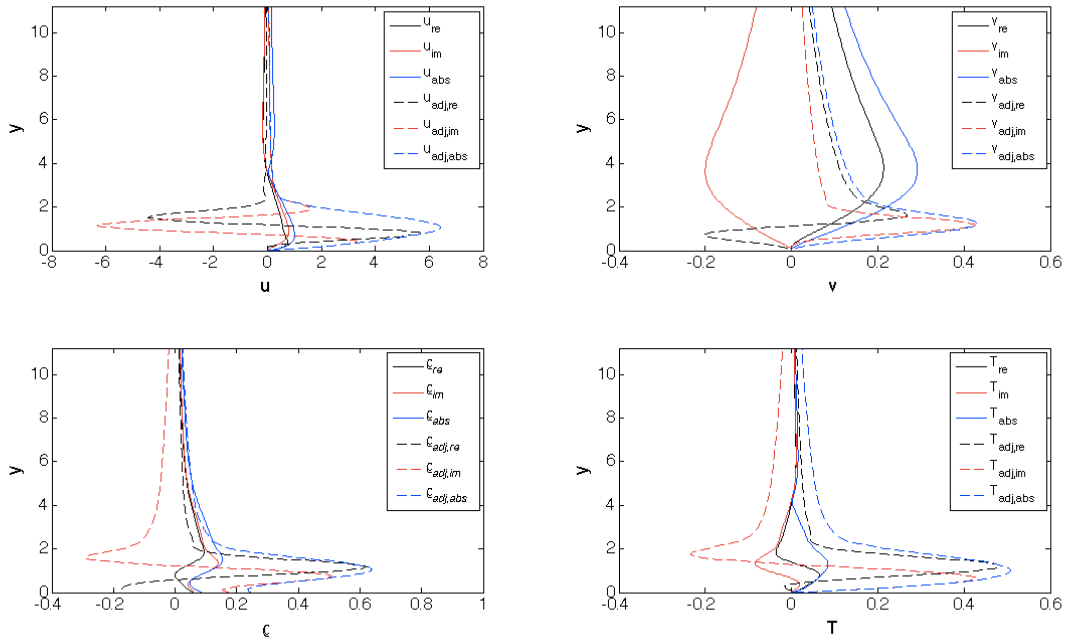

Figure 2.2: Real part, imaginary part and absolute value of the regular and adjoint eigenmodes for M=0.5, Re=1000 and ω=0.046.

Real $\left(\frac{\omega}{\alpha}\right)$ [41] is indicated by dotted lines. A good correlation between the position of maximum adjoint horizontal velocity and this critical layer thickness is observed, as was reported in ref. [1] for incompressible boundary layers. The maximum horizontal adjoint velocity value and position calculated at $M = 0.1$ are in good agreement with the data reported by D. Hill [1] for incompressible flows; see Fig. 2.5(a). When the Mach number is increased, the amplitude of $max|\hat{u}|$ tends to decrease whereas its depth increases with respect to the incompressible case, see example at $M = 0.8$ in Fig. 2.5(b) and further trend in Figure 2.6. A comparison between Fig. 2.7 and Fig. 2.4 indicates a shift in maximum adjoint fields position of the order of 50% between $M = 0.5$ and $M = 1.5$ which as we will see has significant impact on the flow receptivity to forcing for a given geometry. Fig. 2.4 also indicates the Reynolds number as having the strongest influence on the adjoint vertical velocity peak position,

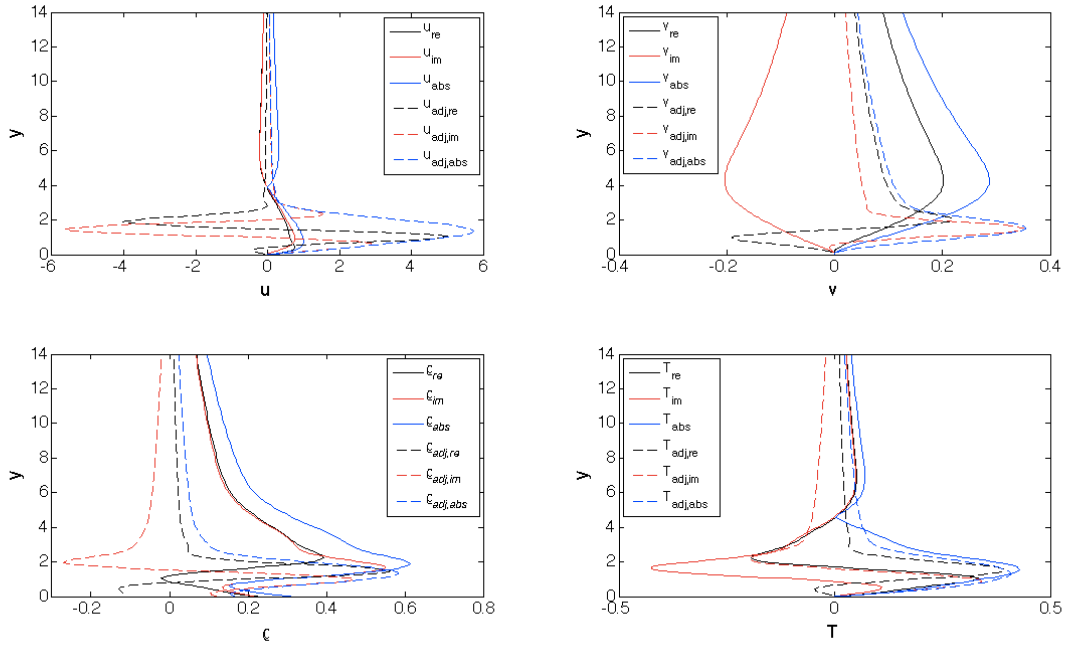

Figure 2.3: Real part, imaginary part and absolute value of the regular and adjoint eigenmodes for M=1.5, Re=1000 and ω=0.036.

with an increase of a factor of two in the considered range. Differently from the other adjoint modes, the vertical adjoint velocity does not show any amplitude minimum versus the forcing frequency ω. At any given frequency where unstable eigenmodes related to different Reynolds numbers coexist, the mode amplitude decreases with decreasing Re, indicating that viscosity has a stabilizing effect on the flow.

2.5 Receptivity analysis

As introduced earlier DBD actuators couple hydrodynamic, electrodynamic, photoionic, thermal and chemical effects of very different time and length scales, and are therefore particularly complex to characterize and model. Numerous studies have been reported and compact modeling of DBD body force and heat components, among others, are the subject of intense research [46–50]. Different actuator geometries

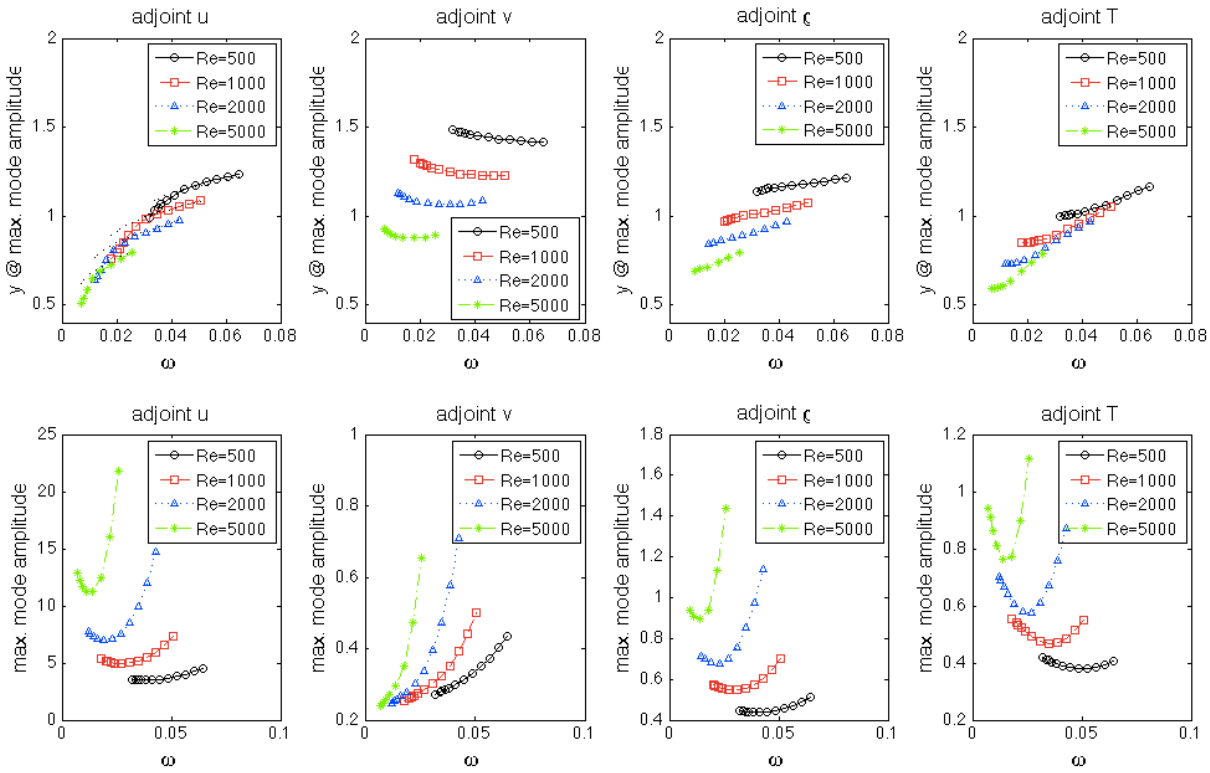

Figure 2.4: Position of the maximum of the absolute value of the adjoint eigenmodes (upper plots, from left to right for $\hat{u}, \hat{v}, \hat{\rho}, \hat{T}$) and corresponding maximum mode amplitude (bottom plots) at $M = 0.5$. In the top/left plot for $\hat{u}$, dotted lines indicate the depth of the so-called critical layer at which the meanflow velocity is equal to $c_r \equiv \text{Real}\left(\frac{\omega}{\alpha}\right)$.

[24, 25, 51] have been considered, with different model approaches including variable forcing volumes affecting drag and moving heat sources [52]. The role of electrode composition, gas chemistry, dielectric permittivity have been investigated [53, 54]. Waveform patterning of the actuating voltage was shown to play a crucial role, for instance in suppressing backward momentum by repetitive short negative pulses over a positive dc bias [55].

In the context of the present quasi-parallel approximation, we aim to investigate the response of the flow to small fluctuations, as a means to gain understanding about the isolated effects of force distribution relative to the flow length scale, viscos-

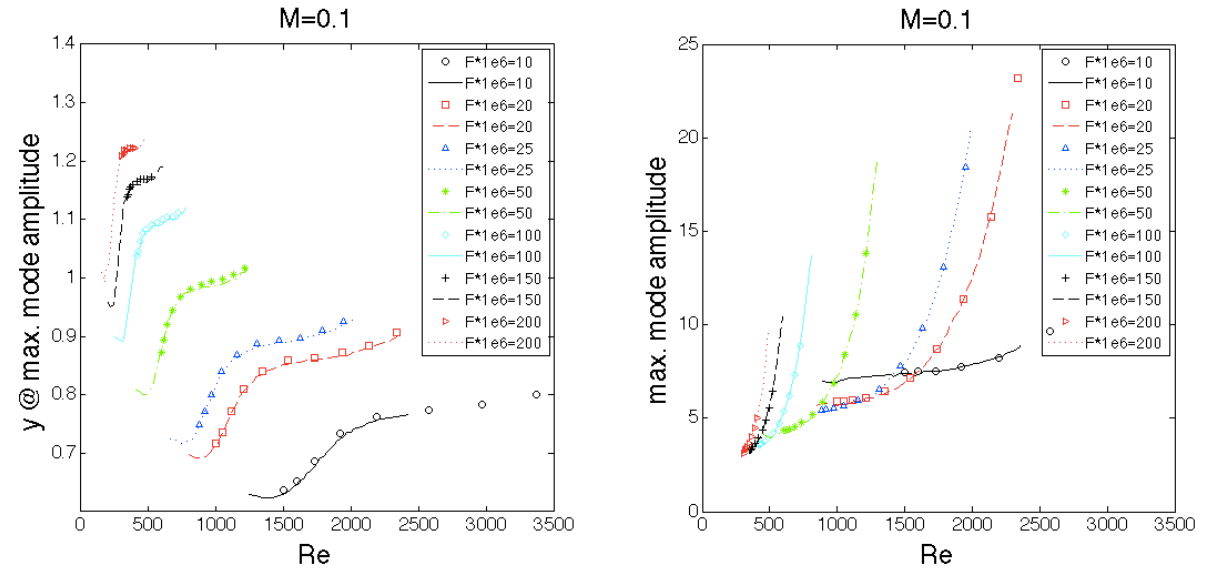

(a)

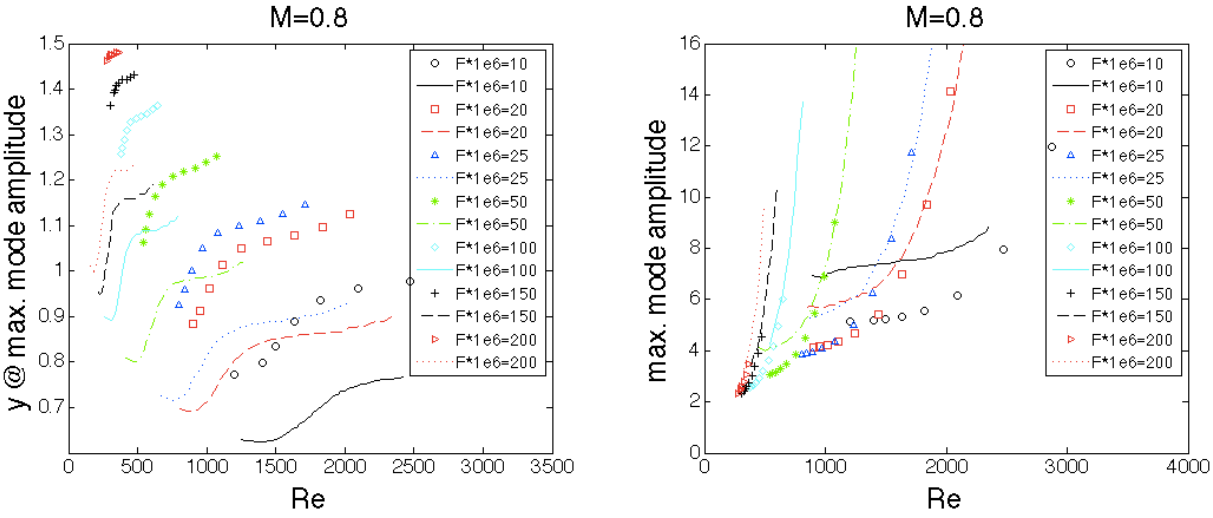

(b)

Figure 2.5: Position (LHS plots) and value (RHS plots) of the maximum of the adjoint horizontal velocity eigenmode $\hat{u}$ versus Reynolds number in the range of frequency $F = \frac{\omega}{\mathrm{Re}}$ reported by D. Hill for incompressible flows [1]. (a) Symbols: this work at $M = 0.1$, lines: data for incompressible flows per ref. [1]; (b) symbols: this work at $M = 0.8$, lines: data for incompressible flows per ref. [1].

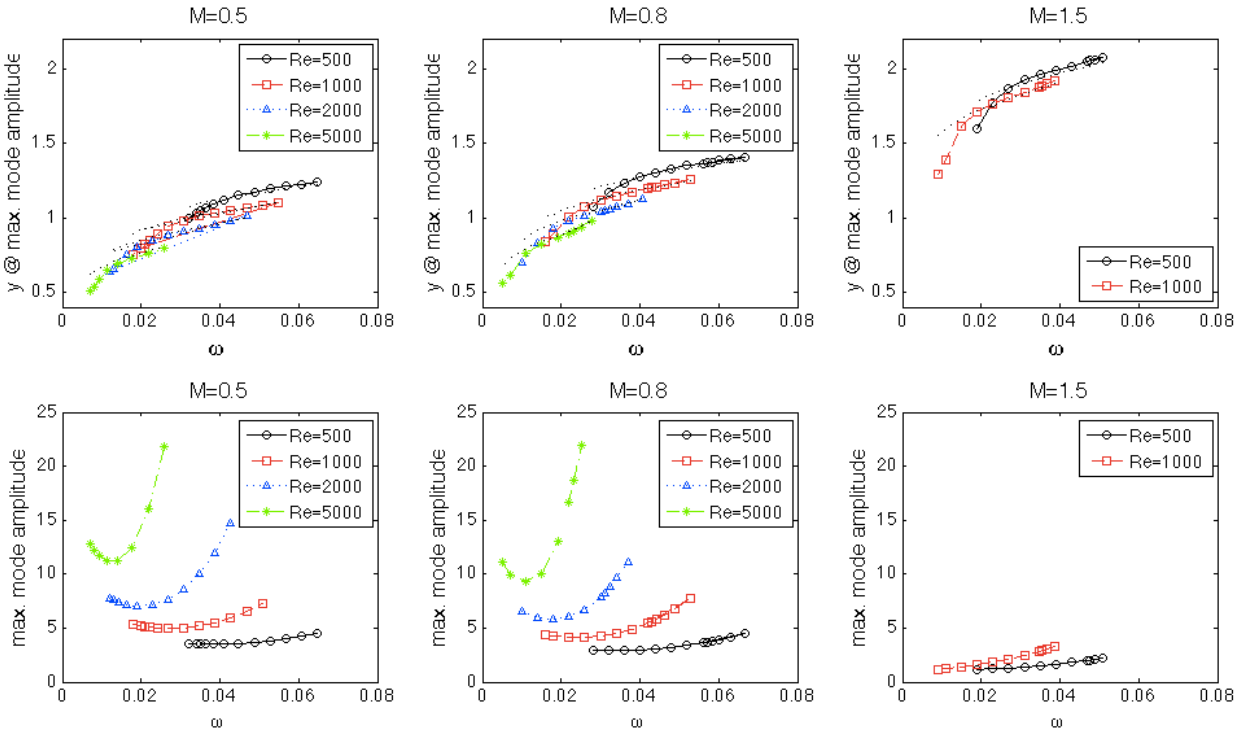

Figure 2.6: Position of the maximum of the absolute value of the adjoint velocity parallel to the flat plate $\hat{u}$ (upper plots) and corresponding maximum eigenmode amplitude (bottom plots) for M=0.5 (LHS), M=0.8 (center) and M=1.5 (RHS). In the top plots the dotted lines indicate the depth of the critical layer.

ity and compressibility. To this purpose we use the analytical force profiles reported in ref. [2, 56]. Other profiles related to different actuator geometries or waveforms could be considered following the same method, see for example ref. [49]. Examples of horizontal, vertical momentum and heat source distributions approximating the result of steady voltage or periodic square pulse applied to DBD actuators are shown in Fig. 2.8 per ref. [2]. These profiles were derived to model signals and flows that vary slowly relatively to the time scale of the DBD cycles of the order of a few μs [2] and constitute a good approximation is low speed flows. The approximation of long hydrodynamic time scale becomes less accurate as the Mach number increases at

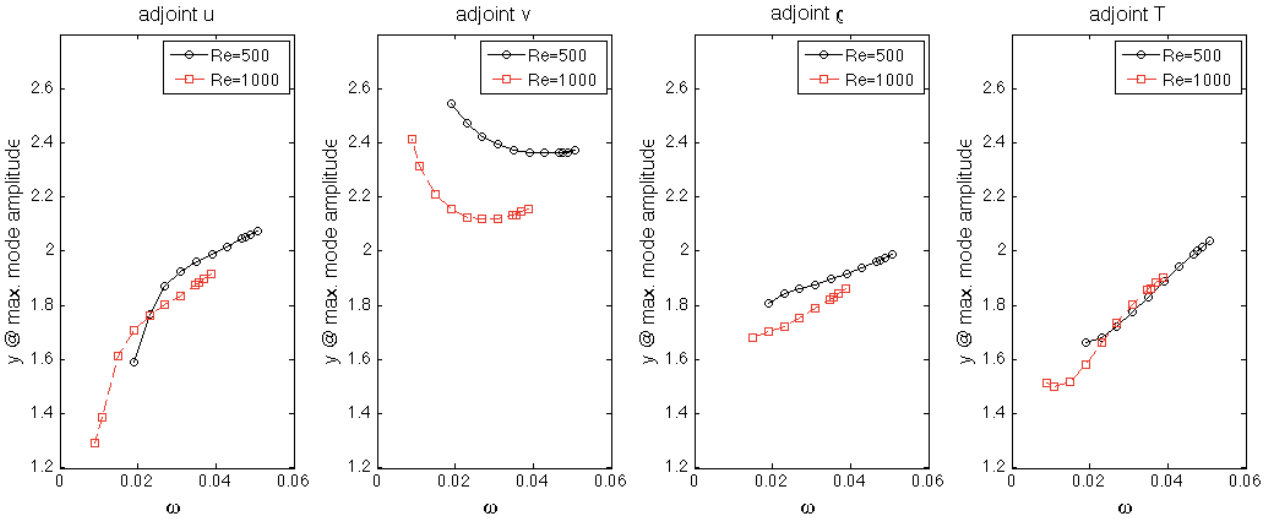

Figure 2.7: Position of the peak of the adjoint eigenmodes (upper plots, from left to right for $\hat{u}, \hat{v}, \hat{\rho}, \hat{T}$) at $M = 1.5$.

constant temperature. For example at $M = 2$, $l_d = 10mm$, and standard conditions, the fluid residence time over the DBD is $\frac{l_d}{u_\infty} \approx 20\mu s$. We do not consider the variations of the source profiles with the freestream conditions, i.e., Reynolds and Mach numbers. As a consequence, the discharge time scale has no influence on the results discussed here, because the linearity of the perturbation problem allows us to analyze independently each frequency of the forcing signal.

On the contrary, the ratio between hydrodynamic and geometrical lengths is an important parameter of the present study, because the adjoint eigenfunctions vary steeply with y, and the location of their largest amplitude identifies the region of the flow that is most sensitive to forcing. The two length scales are varied in 2 ways: A) with fixed actuator dimensions and variable boundary layer (i.e., variable distance between the flat plate edge and actuator leading edge); B) with fixed boundary layer thickness and variable source height, whereas the relative aspect ratio of the sources are kept constant. Following the notations of Fig. 2.8(a), the reference heat and left momentum lengths are given by $l_d = 10mm$, the momentum profile characteristic

height is $h_d = 0.1mm$, and the heat source characteristic height is $h_w = h_d/20$. As illustrated in Fig. 2.8, the profile maxima reach farther into the flow than h_d and h_w due to y factoring in the used analytical profiles [2]. For case A) $y_{max,d} \approx 1.6h_d$ and $y_{max,w} \approx 10h_w \approx h_d/2$, so that the peak position of the heat source profile is about at one third of the momentum maximum. We define the non-dimensional parameter κ as the ratio of the vertical peak position of the momentum profile over the lengthscale L^*.

Figures 2.9-2.11 show the receptivity coefficients obtained from (2.28) for the momentum and heat source profiles of Fig. 2.8(b) representative of steady-state DBD actuating voltage for different forcing frequencies, Mach numbers, κ values and Reynolds numbers while keeping the DBD geometry fixed (i.e., per case A). The TS responses to the individual source terms where only F_x, F_y or Q_s are retained in S_Q of (2.21) and s(x,y) of(2.28) are shown, as well as the sum of all contributions. Under horizontal forcing F_x at Re = 2000 and $M = 0.5$, Figure 2.9 indicates a minimum amplitude at a non-dimensional frequency ω close to 0.03 . Dominance of the horizontal momentum source at low Mach number is understood in terms of the largest amplitude of the adjoint mode $\hat{u}$ in Figure 2.4. Figures 2.10-2.11, which report the maximum receptivity over the range of frequencies ω admitting unstable eigenmodes, indicate a significant decrease ($\approx 1/30$) in peak amplitude with increasing Mach number, in agreement with the trend of Figure 2.6 and Figure 2.1. At Mach 0.5, the peak of the response to F_x is located around $\kappa = 0.8$ which corresponds well with the peak position of the adjoint horizontal eigenmode in Figure 2.6. As the Mach number is increased from 0.5 to 1.8, this peak shifts towards 1.5, following the displacement of the adjoint horizontal velocity $\hat{u}$ in Figure 2.6. Similarly to the F_x case, the left peak of the response coefficients to Q_s (at $\kappa \approx 1.2$ for $M = 0.5, \mathrm{Re} = 2000$) shifts towards

higher values of κ with increasing Mach number, according to the change in overlap of the heat source with the adjoint field $\hat{T}$.

Figures 2.12-2.13 show the receptivity results obtained for harmonic forcing with the source spatial distributions corresponding to the positive and negative half pulses per Fig. 2.8(c) and (d), respectively. For the negative pulse force profile the F_x response does not fulfill the small perturbation assumption. In this case the larger F_y source amplitude translates into larger receptivity coefficients than for the heat source at $M = 0.5$, albeit with larger damping with Mach number. For the positive pulse the horizontal momentum dominates again, with similar trends as observed in the steady-state voltage case.

In case (B), in which the actuator leading edge is kept at a fixed distance from the plate edge and the DBD length scales are varied while keeping the same proportions as the reference design, maximum receptivity is found between $\kappa = 1$ and $\kappa = 2$ at M=0.5 with dominance of the x-forcing source term, that strongly declines in supersonic regime. Careful choice of the actuator position is required to remain in a realistic range of source sizes.

The previous analysis, that was also reported in ref. [57], shows the benefit of matching the actuator excitation profile to the related variable adjoint mode in order to achieve optimum energy transfer.

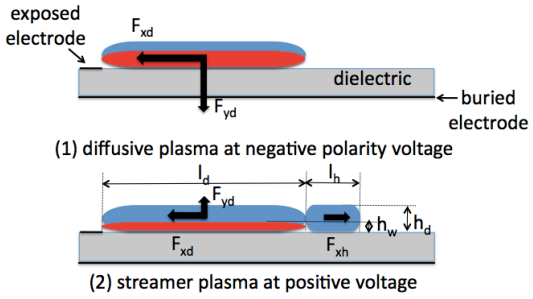

(a) Sketch showing the distribution and sign of the x- and y-components of the body force for (1) diffusive plasma at negative polarity voltage (2) streamer plasma at positive voltage.

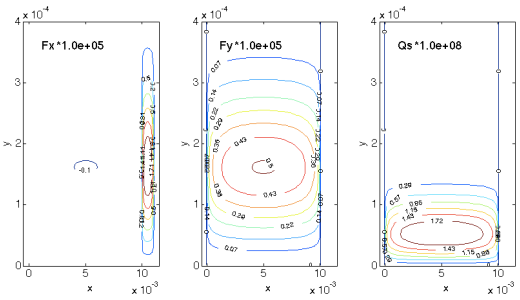

(b) Force distributions representative of steady-state applied voltage.

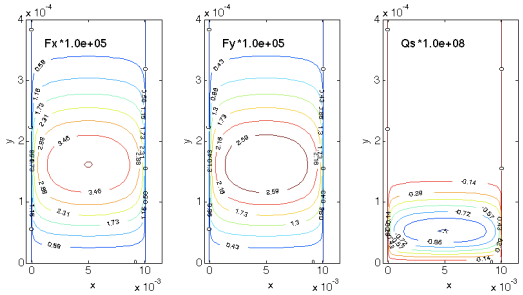

(c) Force distributions reprentative of the negative half period of a periodic square pulse voltage waveform.

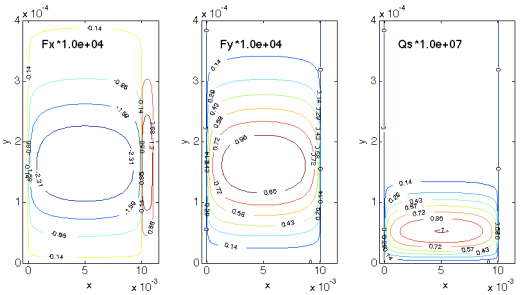

(d) Force distributions representative of the positive half period of a periodic square pulse voltage waveform.

Figure 2.8: DBD actuator horizontal force (F_x), vertical force (F_y) and heat source (Q_s) spatial distributions per ref. [2]. In the present study, these profiles are used as reference amplitudes for single harmonic forcing.

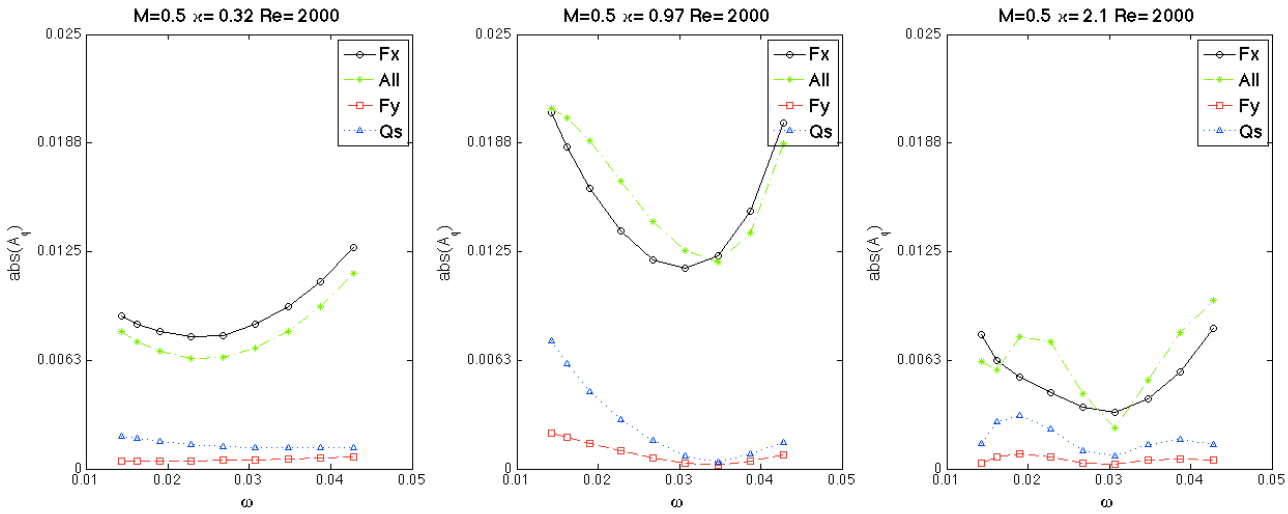

Figure 2.9: Receptivity coefficients resulting from harmonic forcing of F_x, F_y and Q_s amplitude and distribution per Figure 2.8(b) (representative of constant voltage waveform) versus wave number ω at Re $= 2000$, for three length scale ratios $\kappa = 0.32, 0.97, 2.1$ at freestream Mach number $M = 0.5$. Legend *All* corresponds to the sum of all source terms.

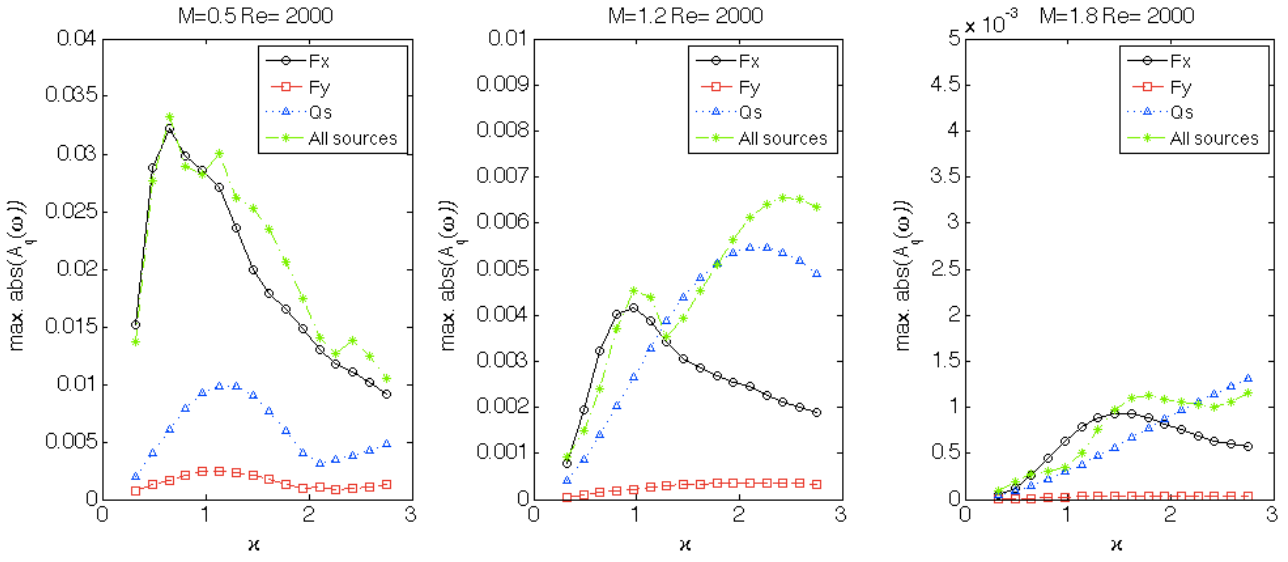

Figure 2.10: Maximum receptivity coefficients (over ω range) at Re $= 2000$ resulting from harmonic forcing of amplitude and distribution per Figure 2.8(b) (representative of steady voltage) versus length scale ratio κ at three freestream Mach numbers ($M = 0.5, 1.2, 1.8$).

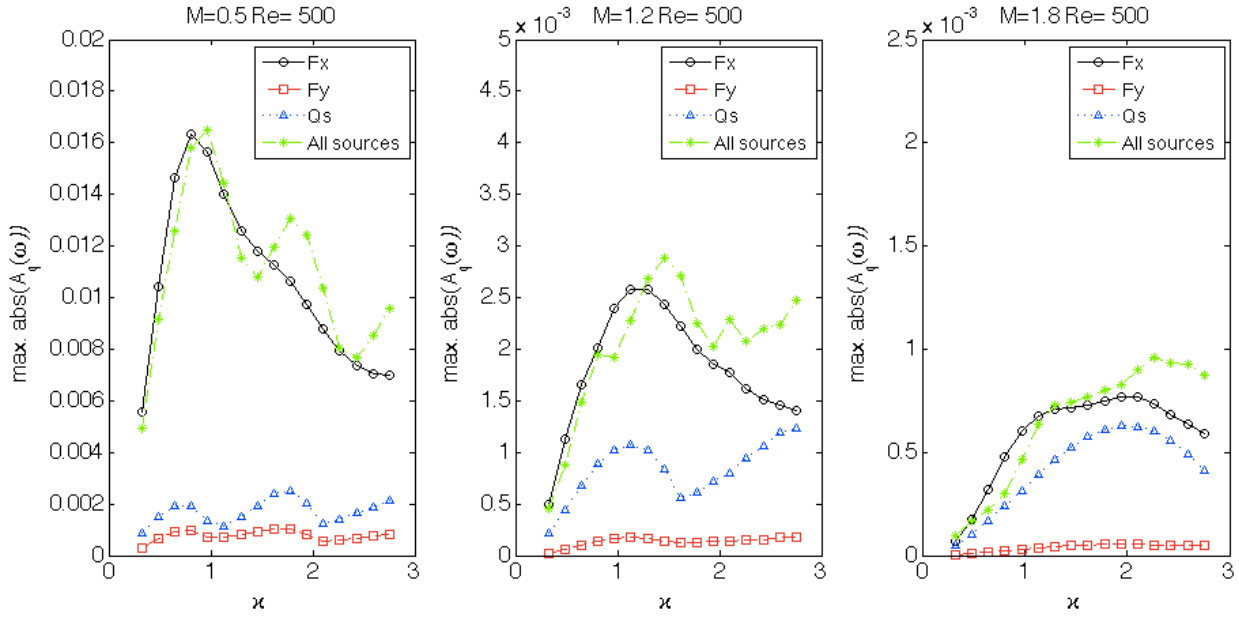

Figure 2.11: Maximum receptivity coefficients (over ω range) at Re $= 500$ resulting from harmonic forcing of amplitude and distribution per Figure 2.8(b) (representative of steady applied voltage) versus length scale ratio κ, at three freestream Mach numbers ($M = 0.5, 1.2, 1.8$).

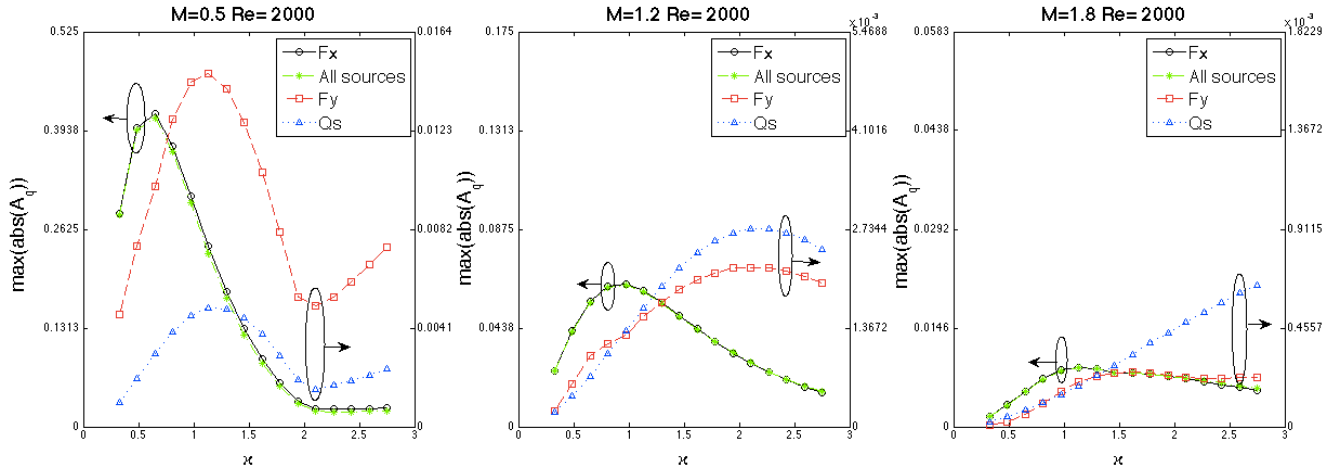

Figure 2.12: Maximum receptivity coefficients resulting from harmonic forcing of amplitude and distribution per Figure 2.8(c) (representative of negative half pulse) at Re $= 2000$, versus length scale ratio κ at three freestream Mach numbers ($M = 0.5, 1.2, 1.8$).

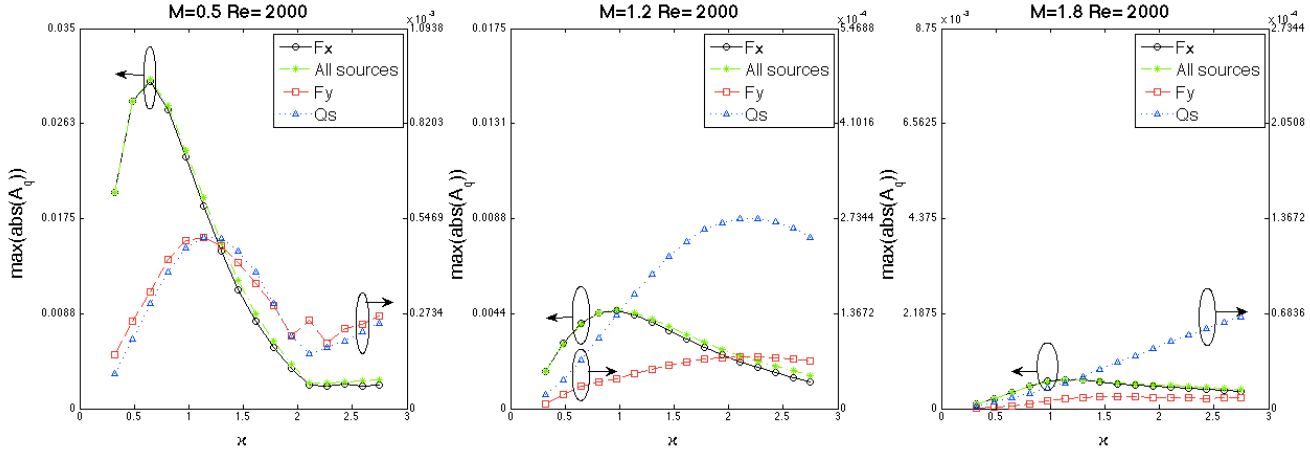

Figure 2.13: Maximum receptivity coefficients at Re = 2000 resulting from harmonic forcing of amplitude and distribution per Figure 2.8(d) (representative of positive half pulse) versus length scale ratio κ at three freestream Mach numbers ($M = 0.5, 1.2, 1.8$).

CHAPTER 3

COUPLED PLASMA-FLUID MODELING

This chapter presents the plasma-fluid models that were implemented in the adaptive mesh refinement framework for the numerical investigation of weakly ionized plasma discharges. A drift-diffusion approximation is assumed, with optional non-equilibrium treatment of the electrons energy. Two chemical models are considered. The first one is a simplified three-species helium system used for the simulation of DC direct discharges. The second second type is an air system accounting for non-equilibrium electron energy, with transport and reaction coefficients dependent on the local electron temperature. The plasma model is coupled to the compressible Navier-Stokes equations through electro-hydro-dynamic force and gas heating source terms, whereas the gas velocity, temperature and pressure are passed to the discharge model.

3.1 Governing Equations

Fluid and particle-fluid hybrid modeling are the two main approaches that have been used to study weakly ionized plasma discharges [58]. Fluid models can be solved following typical CFD methods with some additional stiffness issues caused by the large difference in characteristic time and space scales between the plasma and flow problems. They are overall computationally efficient, but can be limited to qualitative interpretation depending on the validity of the underlying simplifications. Monte-Carlo models on the other hand, allow to simulate the path of indivual particles (such as electrons or selected ions) randomly colliding with the gas, utilizing the fluid

model solution for other species, source terms and for the electric field. The kinetic approach has proven useful to validate fluid models. In spite of being more accurate, it is often computationally costly, although its usage should grow with ever improving computing capabilities and the development of more efficient numerical schemes [36]. The fluid model is expected to serve well the purpose of our studies.

In fluid models, the electron and chemical species are ruled by continuity, momentum and mean energy conservation equations derived from the first moments of the Bolzmann Transport Equation (BTE), which provides the phase-space probability distribution function $g_j(\mathbf{x}, \mathbf{v}, t)$ for species j (electron, ion or neutral) [59]:

$$\frac{\partial g_j(\mathbf{x}, \mathbf{v}, t)}{\partial t} + \nabla . (\mathbf{v} g_j(\mathbf{x}, \mathbf{v}, t)) + \nabla_v . \left[\frac{q Z_j}{m_j} ((\mathbf{E} + \mathbf{v} \times \mathbf{B}) g_j(\mathbf{x}, \mathbf{v}, t) \right] = C_j + S_j \quad (3.1)$$

where m_j is the particle mass, $q = 1.6022 \times 10^{-19} C$ is the electron elemental charge (in absolute value), Z_j the species charge number (=0 for neutral species), C_j represents the scattering effect due to particle collisions and S_j is the external source term. Assuming no magnetic field $\mathbf{B} = 0$, the *Lorentz* force reduces to the force term $q Z_j \mathbf{E}$. The number density, velocity and scalar pressure of species j are mean quantities that can be derived from the probability distribution function integrated in the phase space:

$$n_j = \int g_j(\mathbf{x}, \mathbf{v}, t) d^3\mathbf{v}. \quad (3.2a)$$

$$u_j = \int \mathbf{v} g_j(\mathbf{x}, \mathbf{v}, t) d^3\mathbf{v}. \quad (3.2b)$$

$$p_j = \int m_j \left| \mathbf{v} - \mathbf{u_j} \right|^2 g_j(\mathbf{x}, \mathbf{v}, t) d^3\mathbf{v}. \quad (3.2c)$$

They are called first, second and third moment of $\mathbf{v}$, respectively, and the equations of motion obtained from corresponding integration of the BTE are the fluid-equivalent continuity, momentum and energy equations. The continuity equation reads

$$\frac{\partial n_j}{\partial t} + \nabla . \mathbf{F}_j = \dot{G}_j \quad (3.3)$$

where $\mathbf{F}_j$ is the species number flux and $\dot{G}_j$ is the net rate of generation of species j due to chemical reactions. By assuming that externally induced temporal changes of average momentum and energy density are much slower than inverse scattering rates, the momentum equation is reduced to the following expression of the species flux

$$\mathbf{F}_j = n_j \mathbf{u}_j = sign(Z_j)\mu_j n_j \mathbf{E} - D_j \nabla n_j + n_j \mathbf{V} \tag{3.4}$$

which is called *drift-diffusion* approximation. Here $\mathbf{E} = -\nabla\phi$ is the electric field, which is obtained from the solution of the *Poisson* equation for the electro-static potential ϕ

$$\nabla^2 \phi = -\frac{q}{\epsilon_0 \epsilon_g} \sum_j Z_j n_j \tag{3.5}$$

where $\epsilon_0 = 8.8542 \times 10^{-12} Fm^{-1}$ is the permittivity of free space and ϵ_g is the relative permittivity of the gas (assuming no charge in the dielectric) which is here taken as 1.0055 for air. In (3.4), $\mathbf{V}$ is the bulk flow convective velocity, μ_j is the mobility and D_j the diffusion coefficient. For neutral species,

$$D_j = \frac{k_B T_j}{m_j \nu_{j,g}} \tag{3.6}$$

where k_B is the Boltzmann constant, $\nu_{j,g}$ is the momentum transfer collision frequency [8, 60] and T_j is the species temperature. For a charged species,

$$D_j = \frac{k_B T_j}{q|Z_j|} \mu_j \tag{3.7}$$

In glow discharges, gas heating is usually small enough to assume constant heavy species energy and $T_j = T_g$ where T_g is the local background gas temperature. Differently, the electrons can be heated up to a few electron-Volts and it is necessary to consider a separate temperature. The crudest approach that is sometimes used for DC discharges consists in using a constant value $T_e = \frac{2}{3k_b n_e} e_e$ where e_e is the

average total electron energy. The so-called *local field approximation* (LFA) considers a direct relationship between electron distribution function and electric field, so that the transport coefficients and reaction rate coefficients can be expressed as a function of the local electric field E/N_g where N_g is the background gas concentration. This approximation can yield results in fair agreement with the solution of the non-local electron energy equation, whereby electron diffusivity can be overestimated in the sheath region under high electron density, resulting in an unphysical energy gain when diffusing against the eletric field, which may be overcome by using $-\nabla(D_e n_e)$ instead of $-D_e\nabla(n_e)$ for the diffusion term in (3.4) [35, 61]. A safer, but computationally more intensive option consists in solving for the average electron energy [8, 62]

$$\begin{aligned} \frac{\partial e_e}{\partial t} + \nabla.\left((\frac{5}{3}\mu_e\mathbf{E} + \mathbf{V})e_e - \frac{5}{3}D_e\nabla e_e\right) &= S_e \\ S_e = q\mathbf{F}_e.\nabla\phi - q\sum_j \Delta E_j^e r_j - \frac{3}{2}k_B n_e\frac{2m_e}{m_{k_d}}(T_e - T_g)\nu_{e,g} & \end{aligned} \tag{3.8}$$

where $e_e = \frac{3}{2}n_e k_B T_e$ is the mean electron energy per unit volume. The second term corresponds to the energy variation due to drift and diffusion. In the expression of the electron energy source S_e, the first term is the Joule heating. The second term accounts for inelastic losses in reactions involving electrons, ions, excited species and neutrals, such as ionization, non-resonant charge transfer reactions and energy transfer from electrons to rotational, vibrational and electronic excited states of the neutral gas molecules. ΔE_i^e is the electron inelastic collision energy transfer for reaction i of progress rate r_i. The third term accounts for elastic collisions of electrons with the neutral gas and $\nu_{e,g}$ is the momentum transfer collision frequency with the dominant neutral species of the gas. It is approximated by

$$\nu_{e,g} = \sqrt{\frac{2k_B T_e}{m_e}} N_g \sigma_{e,g} \tag{3.9}$$

where $\sigma_{e,g}$ is the elastic collision cross-sections of electrons to the background gas. The gas energy conservation equation source term reads

$$S_g = \eta_{Th}\left(-q\sum_j Z_j \mathbf{F}_j.\nabla\phi\right) + \frac{3}{2}k_B n_e \frac{2m_e}{m_{k_B}}(T_e - T_g)\nu_{e,g} - q\sum_j \Delta E_j^g r_j \tag{3.10}$$

where η_{Th} is the fraction of ion kinetic energy that is thermalized with the neutral gas. The above source term and the body force

$$\mathbf{f} = -q\sum_j Z_j n_j \nabla\phi \tag{3.11}$$

are coupled to the compressible Navier-Stokes system (2.1)

$$\frac{d\mathbf{U}}{dt} + \nabla.\mathbf{F}_{invisc} = \nabla.\mathbf{F}_{visc} + \mathbf{S} \tag{3.12}$$

where

$$\mathbf{U} = \begin{bmatrix} \rho \\ \rho u \\ \rho v \\ \rho e_t \end{bmatrix}$$

$$\mathbf{F}_{invisc} = \begin{bmatrix} \rho u\mathbf{i} + \rho v\mathbf{j} \\ (\rho u^2 + p)\mathbf{i} + \rho vu\mathbf{j} \\ \rho uv\mathbf{i} + (\rho v^2 + p)\mathbf{j} \\ (\rho e_t + p)u\mathbf{i} + (\rho e_t + p)v\mathbf{j} \end{bmatrix} \tag{3.13}$$

$$\mathbf{F}_{visc} = \begin{bmatrix} 0 \\ \tau_{xx}\mathbf{i} + \tau_{yx}\mathbf{j} \\ \tau_{xy}\mathbf{i} + \tau_{yy}\mathbf{j} \\ (u\tau_{xx} + v\tau_{xy} - \dot{q}_x)\mathbf{i} + (u\tau_{xx} + v\tau_{yy} - \dot{q}_y)\mathbf{j} \end{bmatrix}$$

through the source vector $\mathbf{S}$

$$\mathbf{S} = \begin{bmatrix} 0 \\ \mathbf{f}.\mathbf{i} \\ \mathbf{f}.\mathbf{j} \\ \mathbf{f}.\mathbf{V} + S_g \end{bmatrix} \tag{3.14}$$

3.2 Boundary conditions

The wall boundary conditions for the transport equations take into account thermal and electric species fluxes as [63]

$$\mathbf{F_j}.\mathbf{s} = \alpha_j n_j \mu_j \mathbf{E}.\mathbf{s} + \frac{1}{4} v_{th,j} n_j \tag{3.15a}$$

$$v_{th,j} = \sqrt{\frac{8 k_b T_j}{\pi m_j}} \tag{3.15b}$$

$$\alpha_j = \begin{cases} 1, & sign(Z_j)\mathbf{E}.\mathbf{s} > 0 \\ 0, & sign(Z_j)\mathbf{E}.\mathbf{s} \leq 0 \end{cases} \tag{3.15c}$$

where v_{th} is the species thermal velocity and $\mathbf{s}$ is the unit-vector normal to the surface, pointing towards the outside of the domain. For the electrons, there is an additional flux component to (3.15) from secondary emission of ions and excited radicals impinging onto the solid surface

$$\mathbf{F_e}.\mathbf{s} = \alpha_e n_e \mu_e \mathbf{E}.\mathbf{s} + \frac{1}{4} v_{th,e} n_e - \sum_j \gamma_j \mathbf{F_j}.\mathbf{s} \tag{3.16}$$

where γ_j is the secondary emission coefficient for species j and subscript e refers to the electrons. As shown in ref. [63], the above conditions only partly accounts for diffusion flux to the surface, and may result in unrealistic diffusion of emitted electrons back to the wall, which can be accounted for by articially increasing the secondary emission coefficient (such as by 20% for a 2-species He gas). More accurate conditions can be implemented from information on the fraction of particles reflected at the surface.

Futhermore, charged and excited species that hit the wall are here considered to recombine at the surface with a sticking coefficient of one. The species flux across the upper boundary of the domain is zero. The inflow fluxes $\mathbf{F_j}.\mathbf{s}$ are calculated as Dirichlet conditions from (3.4) using the upstream initial species concentrations, whereas species are convected out of the domain with $\mathbf{F_j}.\mathbf{s} = n_j\mathbf{V}$.

The electron energy flux at the wall is given by

$$\mathbf{F_{ee}}.\mathbf{s} = \epsilon_w \mathbf{F_e}.\mathbf{s} - \epsilon_{\gamma e} \sum_j \gamma_j \mathbf{F_j}.\mathbf{s} \tag{3.17}$$

where ϵ_w is taken as $2k_BT_e$ under the assumption of a Maxwelian electron distribution function per ref. [8] and $\epsilon_{\gamma e}$ is estimated from the ionization energy ϵ_z, surface work function ϵ_ϕ and electrode Fermi energy ϵ_F as $\epsilon_{\gamma e} = \epsilon_z - 2\epsilon_\phi - \epsilon_F$. Like for the species the inflow energy flux is treated using the upstream starting concentrations and the outflow flux is extrapolated from the interior field, whereas the upper domain limit is treated as reflective boundary.

The gas wall boundary condition is adiabatic and as earlier the flux is zero at the upper boundary. The gas inflow fluxes are defined from the solution of a Navier-Stokes similar system described in ref. [64] assuming a non-zero momentum thickness at the inflow, that is used as an input parameter to study the influence of the boundary layer thickness using a fixed geometry.

For the solution of the electrostatic potential the electrodes are treated as Dirichlet boundaries. The implemented alogorithm offers the capability of accounting for the surface charge at the dielectric/gas interface solved from the ODE

$$\frac{\partial \sigma_s}{\partial t} = q \sum_j Z_j \mathbf{F_j}.\mathbf{s} \tag{3.18}$$

The surface charge σ_s and resulting dielectric displacement are used as boundary condition to solve for the electro-static potential

$$(\epsilon_g \nabla\phi - \epsilon_d \nabla\phi_d).\mathbf{s} = \sigma_s \tag{3.19}$$

where indices g and d refer to the gas and dielectric sub-domains. Continuity of the tangential component of the electric field requires additionally

$$(\nabla\phi_g - \nabla\phi_d).\mathbf{t} = 0 \tag{3.20}$$

where $\mathbf{t}$ is a unit vector tangential to the dielectric surface. The other boundaries are set to a Neumann type, depending on the electrode and dielectric geometry a Dirichlet solution from the asymptotic value of an analytical solution can be used [35].

3.3 Air model

Various air plasma models have been proposed within the local field approximation. For example K. Singh proposed in ref. [33, 47] an 8-species, 8-reactions model assuming a Boltzmann electron distribution to calculate the electron temperature from $\mathbf{E} = k_B T_e/(\nabla n_e/n_e)$ with transport coefficients from ref. [65] and reaction rates from ref. [66]. For very fast signal variations such as under nano-second pulse DBD operation, a dedicated set of parameters was proposed in ref. [32, 34] with 4 species, 5 reactions with rates, tranport coefficients and local electron temperature dependent on E/N_g where N_g is the background gas concentration. In [35] V. Soloviev considered 9 species and 8 reactions with ion and electron temperatures dependant on the electric field, and an extra species source term due to the photo-ionization of O_2 molecules by UV radiation of excited N_2 molecules. Also included in this model and in ref. [2] is a non-local correction of the ionization rate coefficient to account for diffusion against the electric field in the sheath region.

The air plasma model by S. Mahadevan [8] was implemented in our new AMR flow-plasma solver. It includes 11 species and 21 reactions per Table 3.1, reactions $\#5-6$ of which represent lumped reactions used as energy sinks to account for the electron energy inelastic loss due to rotational, vibrational and electronic excitation of ground state of N_2 and O_2. N_2 and O_2 densities have fixed mole fractions of 0.79 and 0.21, respectively. The reaction rates involving electrons were extracted as a function of electron temperature by means of the zero-dimensional Boltzmann equation solver BOLSIG+ [67]. For this the fitting parameters reported in ref. [8] were used, as well as alternate fits with ionization level varied in the range $[10^{-6}, 10^{-4}]$. The functions used for the corresponding reaction rate coefficients k_j are of the type $ln(k_j) = \sum_{j=0}^{\leq 9} c_j/T^j$ and an example is given in Figure 3.1 for nitrogen ionization (=reaction #1 in Table 3.1). The electron mobility was also extracted with BOLSIG+ [67], using a function of the type $ln(N_g\mu_e) = \sum_{j=0}^{8} c_j ln(T_e)^j$, see Figure 3.2.

The ion mobilities $\mu_j N_g$ were obtained as a function of the local electric field E/N_g from ref. [3, 65, 68, 69], using the same type of function as for the electron mobility, see for example Figure 3.3 for N_2^+. All fits were bounded in the plasma-flow solver, so that calculated values remain within the range of extracted values. For example, mobility values for $E/N_g = 1Td = 1 \times 10^{-21}[Vm^2]$ were used for any values lower than this threshold. The momentum transfer collision frequency $\nu_{j,g}$ was fitted to the data reported in ref. [4, 5] for nitrogen and oxygen, using a triple Gaussian fit, see Figure 3.4.

3.4 Helium model

The reduced Helium model reported in ref. [31] is limited to ionization and recombination. Excitations, ionization by excited atoms, ion coversion and de-excitation processes are not considered. It was implemented here as a convenient tool for basic

	Reaction	**Rate Coefficient** $[m^{3(n-1)}s^{-1}]$	ΔE^e $[eV]$	ΔE^g $[eV]$	**Ref.**
1	$e + N_2 \rightarrow 2e + N_2^+$	BOLSIG+	15.6		[67]
2	$e + O_2 \rightarrow 2e + O_2^+$	BOLSIG+	12.07		[67]
3	$e + O_2 \rightarrow > e + 2O$	BOLSIG+	5.58		[67]
4	$e + O_2 \rightarrow e + 2O$	BOLSIG+	8.4	-2.82	[67]
5	$e + O_2 \rightarrow O + O^-$	BOLSIG+	3.6		[67]
6	$e + N_2 \rightarrow e + N_2$	BOLSIG+	1	-1	[67]
7	$e + O_2 \rightarrow e + O_2$	BOLSIG+	1	-1	[67]
8	$e + O_4+ \rightarrow 2O_2$	$2.42 \times 10^{-11} T_e^{-0.5}$		-12.7	[66]
9	$e + O_2+ \rightarrow O_2$	$6 \times 10^{-11} T_e^{-1.0}$		-6.91	[66]
10	$e + 2O2 \rightarrow O_2 + O_2^-$	$6 \times 10^{-39} T_e^{-1.0}$		-0.43	[66]
11	$O_2 + N_2+ \rightarrow N_2 + O_2^+$	$1.05 \times 10^{-15} T_g^{-0.5}$		-3.51	[66]
12	$2N_2 + O_2^+ \rightarrow O_2^+ N_2 + N_2$	$8.1 \times 10^{-38} T_g^{-2.0}$			[66]
13	$O_2^+ N_2 + N_2 \rightarrow 2N_2 + O_2+$	$14.8 T_g^{-5.3} e^{\frac{-2357}{T_g}}$			[66]
14	$M + O_2 + O_2+ \rightarrow M + O_4^+$	$2.03 \times 10^{-34} T_g^{-3.2}$			[66]
15	$O_2^- + O_4^+ + M \rightarrow 3O_2 + M$	$3.12 \times 10^{-31} T_g^{-2.5}$			[66]
16	$O_2^- + O_2^+ + M \rightarrow 2O_2 + M$	$3.12 \times 10^{-31} T_g^{-2.5}$			[66]
17	$O^- + O_2^+ \rightarrow O + O_2$	$3.46 \times 10^{-12} T_g^{-0.5}$		-10.61	[66]
18	$N_2^+ + N_2 + M \rightarrow N_4^+ + M$	5×10^{-41}			[66]
19	$N_4^+ + O_2 \rightarrow O_2 + +2N_2$	2.5×10^{-16}		-3.51	[66]
20	$O_2 + N_2 + O_2 \rightarrow O_4^+ + N_2$	1×10^{-15}			[66]
21	$O_2^- + O_4^+ \rightarrow 3O_2$	1×10^{-13}		-11.64	[66]

Table 3.1: *Air chemistry system per [8].*

discharge analysis and program development. In this model continuity equations for the electrons and helium ions read

$$\frac{\partial n_j}{\partial t} + \nabla.\mathbf{F_j} = \dot{G}_j = r_z n_e - r_r n_e n_i, \quad j = e,\ i \tag{3.21}$$

where n_e is the electron concentration and n_i is the helium ion concentration. The ionization rate r_z and recombination rate r_r are given by ref. [31, 70]

$$r_z = \alpha \mu_e E \tag{3.22a}$$

$$\alpha = 3.3 exp\left(\frac{-12.479}{(E/P)^{0.4}}\right) P \mu_e E \tag{3.22b}$$

$$r_r = 1.12 \times 10^{-7} + 2.2 \times 10^{-33} N_g \tag{3.22c}$$

Secondary electron emission is assumed at the electrode with coefficient $\gamma_e = 0.23$ ref. [6]. Differently from ref. [31] the electron mobility was extracted from BOLSIG+

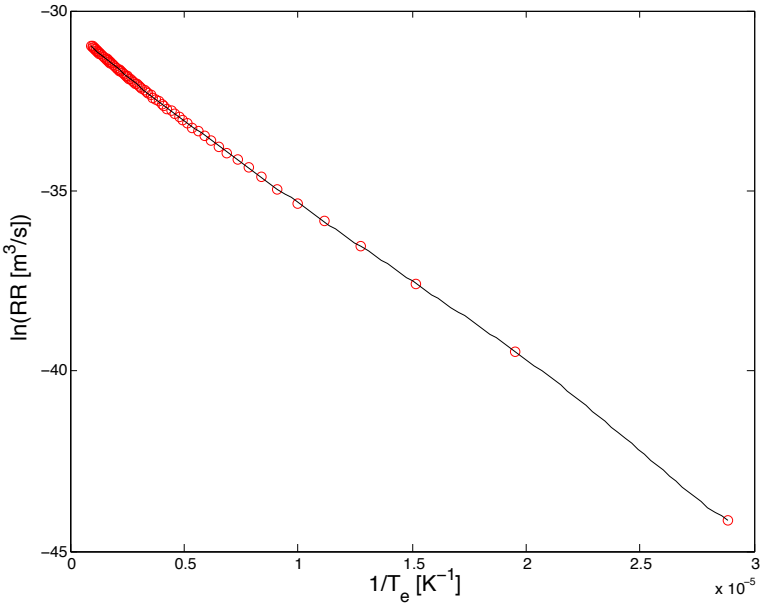

Figure 3.1: Nitrogen ionization reaction rate coefficient calculated with BOLSIG+, assuming 1×10^{-4} ionization degree and 0.79/0.21 N_2/O_2 gas fractions (symbols), and corresponding fit (line).

whereas the Helium ion mobility in Helium gas was fitted from data reported in ref. [65]. The electron temperature can be fixed (e.g. to 1 eV as typical for glow discharge) or T_e can vary per (3.8), in which case above ionization rate is calculated based on a BOLSIG+ extraction. Figure 3.6 shows an example of zero-dimensional simulation in Matlab, considering a single cell with boundary conditions per prior section applied at opposite faces. The value of the electric field is 6×10^5, which is above the minimum threshold for helium breakdown, see Figure 3.5 with *Paschen*'s curve for the selected pressure of 300 Torr. Starting from a background electron concentration of $1 \times 10^4 m^{-3}$ and zero ion concentration, the species concentrations in the cell increase until the ionization and recombination rates become equal. The electron concentration at steady state is lower than the ion concentration due to assumed recombination at the wall and larger electron mobility. An interesting feature

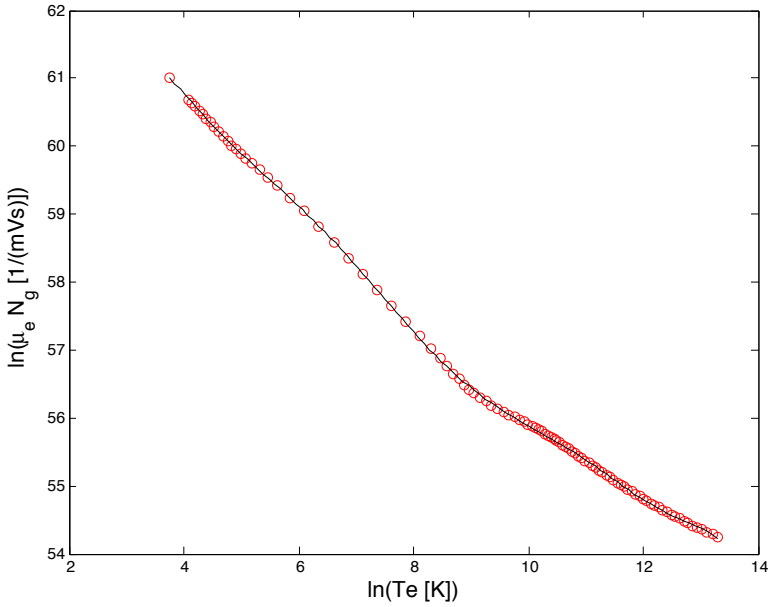

Figure 3.2: Fit (line) of the electron mobility data (symbols) calculated with BOLSIG+, assuming 1×10^{-5} ionization level and 0.79/0.21 N_2/O_2 gas fractions.

of Figure 3.6 relates to the stability of this simple system: since the ionization slope vs. n_e is smaller than for recombination, deviation from equilibrium in the form of an electron density increase will be damped by recombination [6].

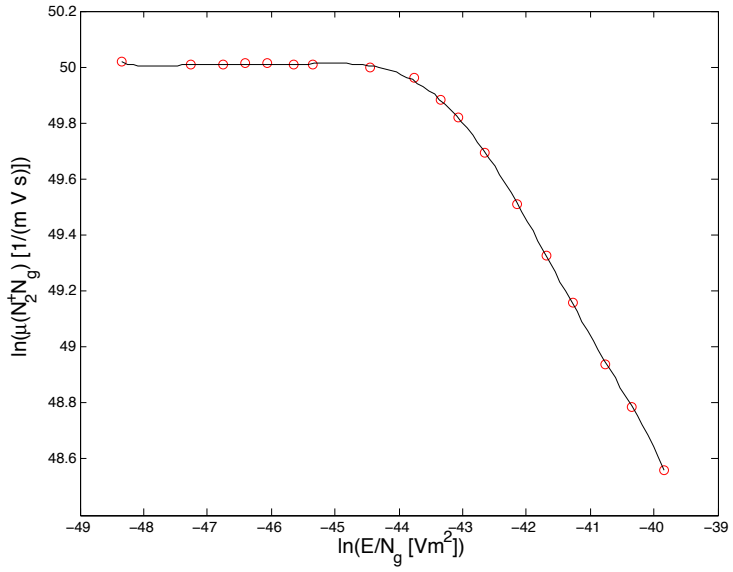

Figure 3.3: N_2^+ ion mobility fit to data from ref. [3].

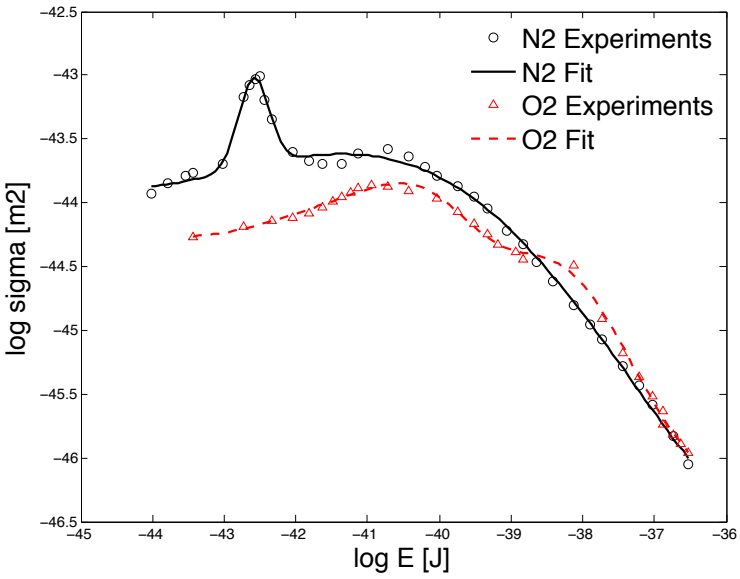

Figure 3.4: Electron-nitrogen and electron-oxygen elastic collision cross-section data per ref. [4, 5] and corresponding fitting.

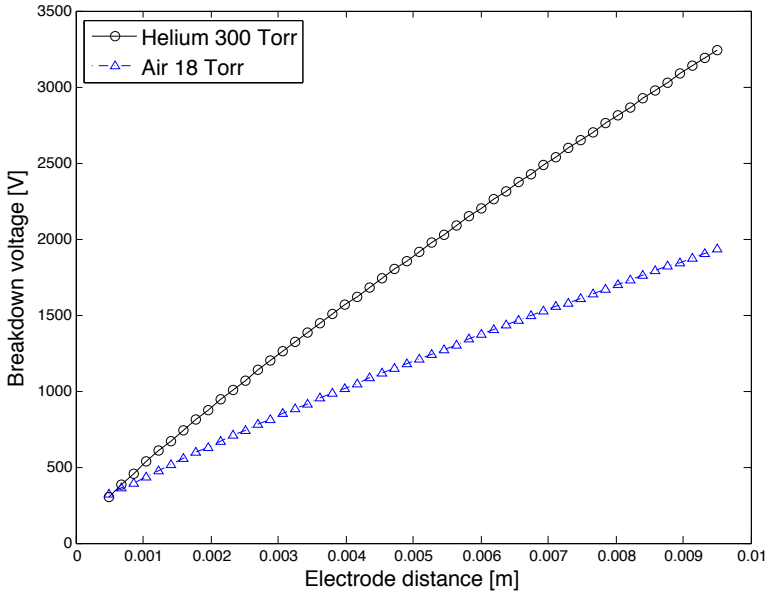

Figure 3.5: Constant pressure *Paschen* curve for minimum breakdown voltage in air and helium [6, 7].

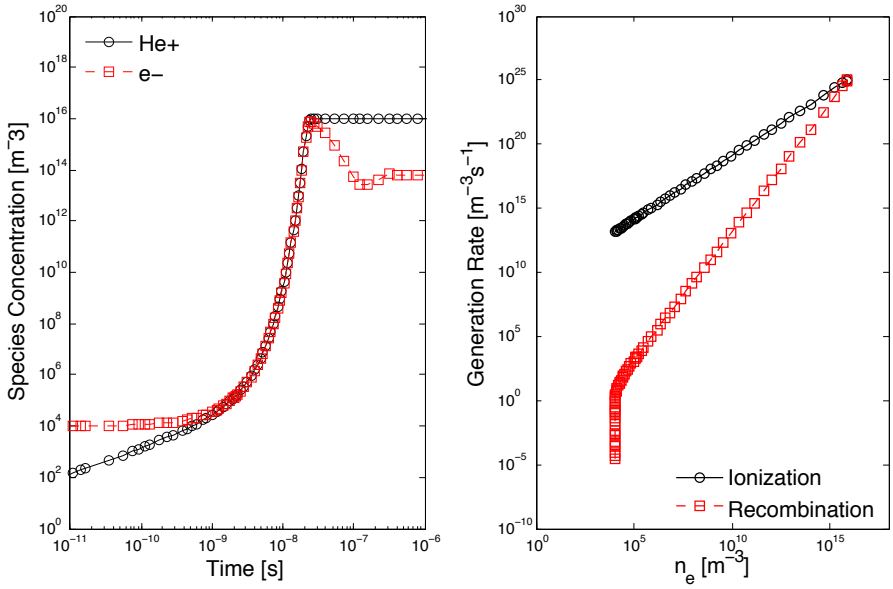

Figure 3.6: Zero-dimensional, 1-cell Matlab simulation for an helium model ($E = 6 \times 10^5 V/cm$).

CHAPTER 4

AMR PLASMA-FLOW SOLVER

In this chapter we describe the coupled plasma-flow solver developed for the investigation of DBD actuators. The plasma solver development involves the definition of a mixed dielectric-gas domain separated by a seamless embedded boundary, a Poisson solver with mixed-mode boundary conditions accounting for the electrodes and dielectric layer, and a plasma physics module computing the species chemical source terms, electron and gas energy source terms, transport coefficients and charge fluxes at the wall. The chapter is organized as follows: the adaptive mesh refinement framework is first introduced, then the plasma-flow coupling algorithm is discussed, the sharp-interface immersed boundary conditions are explained, and, finally the plasma physics module is described.

4.1 AMR Algorithm

The *Chombo* C++ framework for the finite volume solution of partial differential equations is chosen as platform for the new solver [71]. The algorithm allows to solve efficiently steady state and time dependent systems in complex domains involving multiple scales and embedded boundaries. It uses block-structured Adaptive Mesh Refinement (AMR) to solve multi-scale partial differential equations. In this approach the problem domain is recursively discretized using a rectangular grid that is locally refined by an integer factor over a disjoint set of boxes based on some measurable error. In the Embedded Boundary (EB) algorithm, the index space is the hierarchy of

rectangular lattices combined with a graph representing the irregular cell fragments that abut the irregular boundary, where the successive members of the hierarchy are related to one another by coarsening and refinement operations. Operations are executed as a loop over stencil locations, with three types of cells: regular, irregular (abutting the EB from the inside of the domain) and covered (outside of the problem domain).

4.2 Plasma-flow solver architecture

The Navier-Stokes (NS) code was developed and extensively validated in prior research [72]. The integrated flow-plasma solver utilizes an operator split algorithm with two main branches: the Navier-Stokes solver and the species and electron energy update (plasma), see Fig. 4.2. Exchanges between the main branches are performed at the end of a time-step and include passing of source terms from the plasma to the NS solver and fluid variables in the opposite way. In the adaptive mesh refinement algorithm the coupling can be performed in a tight way, meaning within the time-subcycling, or in a loose way, at the end of a coarse time step. The plasma and fluid modes are loosely coupled in the present algorithm. The Navier-Stokes solver is a second order semi-implicit fluid solver with a Godunov-type approximation of the inviscid fluxes. The well known flux limiter formulation due to van Leer is used in for the inviscid fluxes. The viscous part of the Navier-Stokes equations is discretized using a cell-centered finite difference scheme. The plasma equations (i.e., those including species concentration and electron energy) are in turn solved by an operator splitting procedure. The convective term in the species equation is discretized using the second order Godunov approach applied to the passive scalars. The diffusive terms, including the mobility contribution, are discretized using an implicit Backward-Euler method. The chemistry source terms are integrated using a fifth order stiff ODE solver. Finally,

the elliptic Poisson equation is solved using a Multigrid algorithm with Gauss-Seidel relaxations and the biconjugate gradient stabilized method as the bottom solver of the V cycles. Note that the decoupling between source and diffusive terms, which are both handled implicitly, is necessary to simulate the plasma equations with fast ion reactions, whereby chemical time-scales of the order of the picosecond are introduced.

4.3 Boundary conditions for the electro-static potential

In some cases a thin dielectric analytical approximation can be used to estimate the potential at the interface between the gas and the dielectric layer. It is advantageous to accurately solve for the dielectric region as the electrode edges are subject to strong electric fields and carrier distribution at the dielectric interface can influence the discharge significantly. Moreover this capability allows investigating integrated, stepped electrodes and non-idealities of the dielectric, which at present is considered as charge-free. Here, the dielectric region is integrated into the solution domain by taking advantage of the embedded boundary formalism. Usually in Chombo the EB lies along covered cells, 1D EB boundaries in 2D domains or plane boundaries in 3D domains are special configurations that the software can handle but that are not predefined. In order to implement the EB at the dielectric/gas boundary, a slab made of two rows of covered cells is defined, the covered cells interface at the desired wall position. In a next step, the covered cells are transformed into irregular cells, and a zero area fraction is attributed to the bottom face of the cells in the top row and to the top face of the cells in the bottom row, which lets Chombo handle these faces like the boundaries to a thickness-less covered domain.

The electrodes at the dielectric surface necessitate the definition of mixed Dirichlet-Neumann boundary conditions both for the domain (bottom electrode) and the embedded boundary (top electrode). Here the Poisson solver's Neumann and Dirichlet

boundary routines are integrated and made functions of position according to the definition of the wall and electrode geometry. Condition (3.19) is nor Neumann nor Dirichlet and require special handling. It is implemented by combining a pseudo-Dirichlet with a stencil manipulation as follows. The vertical derivative of the electrostatic potential at the wall can be expressed as the sum of a surface value, plus a function of the stencil associated to the cell:

$$\frac{\partial \phi_s}{\partial y} = \phi_s W_{g,d} \alpha_{g,d} \kappa + \Psi_{g,d}(\phi) \tag{4.1}$$

where subscript s indicates the wall surface, W is a weight coefficient, α is the wall cell face area fraction, κ is $\frac{1}{dx}$ and Ψ is a function of the ϕ solution inside of the domain, with g or d indicating the side (gas or dielectric) of the EB. By using (4.1) in (3.19) one obtains the following expression for the surface potential

$$\phi_s = \frac{\sigma_s}{(\epsilon_d W_d \alpha_d - \epsilon_g W_g \alpha_g)\kappa} - \frac{\epsilon_d \Psi_d(\phi) - \epsilon_g \Psi_g(\phi)}{\epsilon_d W_d \alpha_d - \epsilon_g W_g \alpha_g} \tag{4.2}$$

The first term of (4.2) is used as Dirichlet condition at the EB, whereas the second term is incorporated to the stencil. The solution was validated on analytical cases and a simulation example is shown in Fig. 4.1. When integrated with the plasma solver, ρ_s is to be passed to the boundary routine from the solution of (3.18).

4.4 Plasma physics module

The plasma physics module computes the chemical species source terms, the energy source terms for the electron and gas, the forcing terms for the Navier-Stokes system, and the charge flux at the wall according to the models presented in Chapter 3. The source terms are obtained from the calculation of the reaction rates and local concentrations

$$S_j = \sum_r \nu'_{r,j} k_r \prod_s n_s^{\nu_{r,s}} \tag{4.3}$$

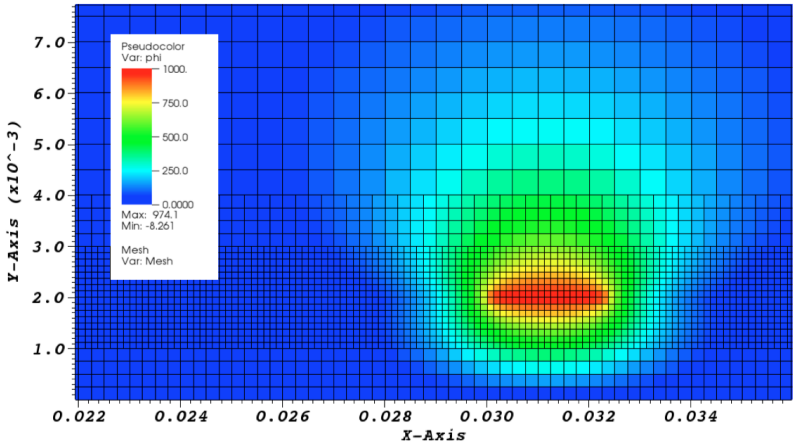

Figure 4.1: Poisson equation multi-grid solution example in the hybrid dielectric-gas domain using surface charge correction per (4.2) at the EB, with mixed Neumann/Dirichlet boundary conditions and 1000V applied at the EB electrode.

where r iterates over all reactions, s iterates over all species, $\nu_{r,s}$ is the reactant stoechiometric coefficient for species s in reaction r, $\nu'_{r,s}$ is the net reaction stoechiometric coefficient for species s in reaction r, and k_r is the reaction rate coefficients for reaction r. All parameters are implemented as species and reaction indexed arrays in a parameter routine so that the chemical model can be easily modified.

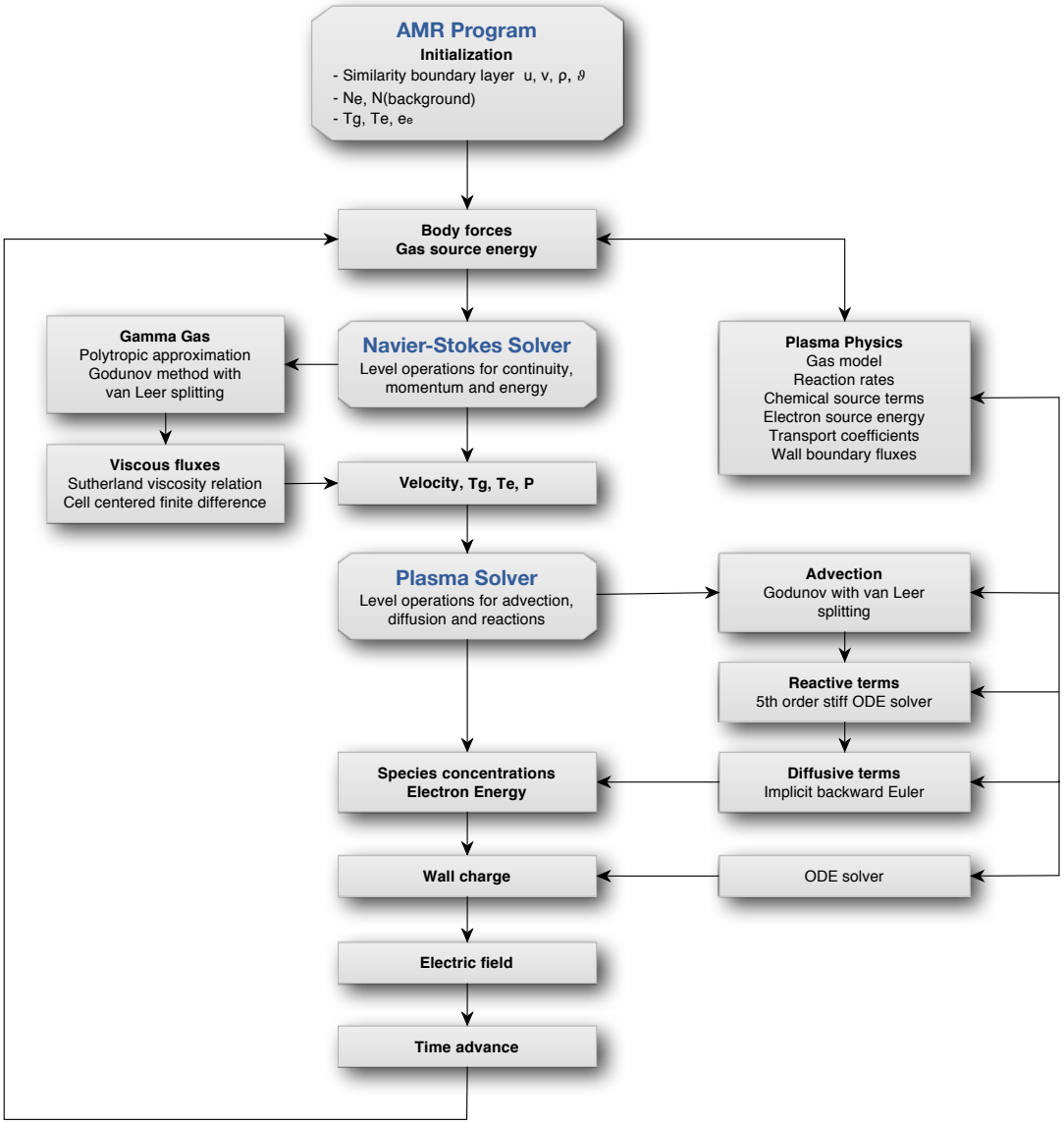

Figure 4.2: Solver flow chart

CHAPTER 5

PRELIMINARY SIMULATION RESULTS

This chapter describes simulation results obtained for a set of discharge conditions aimed to investigate the effect of compressibility and Damköhler number on the plasma force profiles. The results presented herein are preliminary in the sense that a simplified gas model is used under the assumption of constant electron temperature.

5.1 Helium Direct Discharge

The program is tested with direct discharges using the helium system outlined in Chapter 3. Constant electron temperature is assumed with $T_e = 1eV$. A fixed mesh of cell size of $250\mu m$ is used in all calculations reported. The domain is $50 \times 10cm$ with an electrode spacing of about 5mm. The cathode is placed at the left hand side (upstream), and the applied DC voltage is -3000V, see Figure 5.1. Subsonic and supersonic boundary layers are considered with inflow Mach number varied between 0.8 and 3.0. The far field pressure is 300 Torr. The mean flow is the solution of a self-similar adiabatic boundary layer profile, with momentum thickness θ at the inflow boundary varied between 1×10^{-4} and 1×10^{-3} m. The non-dimensional Reynolds number is 7×10^4, the Prandtl number is 0.72 and the specific heat capacitance ratio is given by $\gamma = c_p/c_v = 1.4$.

Figure 5.2 shows the ion distribution for the different flow conditions. The convective horizontal velocity at $M = 0.8$ in the cathode area of the glow is about $100ms^{-1}$, which is about one order of magnitude lower than the ion drift velocity $\mu E \approx$

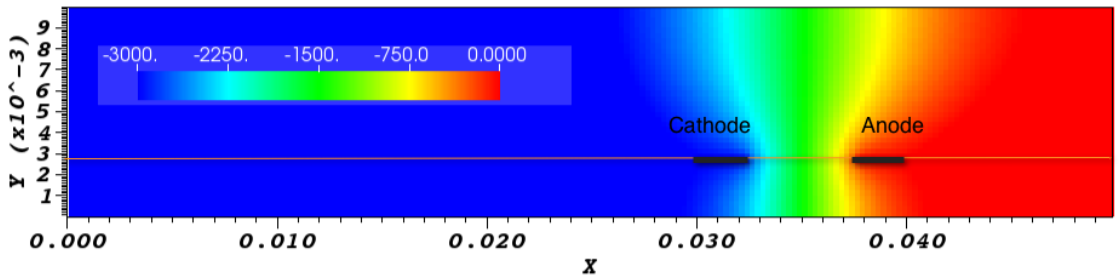

Figure 5.1: Simulation domain and electrostatic potential field for the direct discharge computations.

$900ms^{-1}$. Some convection is observed at the edge of the discharge in the $M = 3$ case, where the flow velocity becomes comparable to the drift velocity in the electric field. For the supersonic cases the peak ion concentration at the cathode edge is about five times larger than for subsonic flow, whereas the electron concentration is significantly lower (about half between the electrode and 30% at the anode), Figure 5.3. The horizontal force excercised by the plasma is insensitive to the selected flow conditions, see distribution for $M = 0.8$ in Figure 5.4. The vertical force is more than twice larger at the cathode for the high speed cases, consistently with the larger charge concentrations noted above. Under the considered adiabatic wall boundary condition, the boundary layer temperature at the wall is $T_{g,wall} = 345,\ 728,\ 775K$ at $M = 0.8,\ 1.5,\ 3.0$, respectively. In the model used, temperature affects the ion diffusion coefficient and the wall species thermal flux component linearly, and could be the cause of the increased discharge current. With the exception of the region immediately adjacent to the electrodes, similar discharge structure and force terms are seen across the test cases, which would support the assumptions taken in the receptivity study of chapter 2 for this particular system. Further work is planned, that will exploit the refinement capabilities of the solver to improve the resolution of the cathode sheath

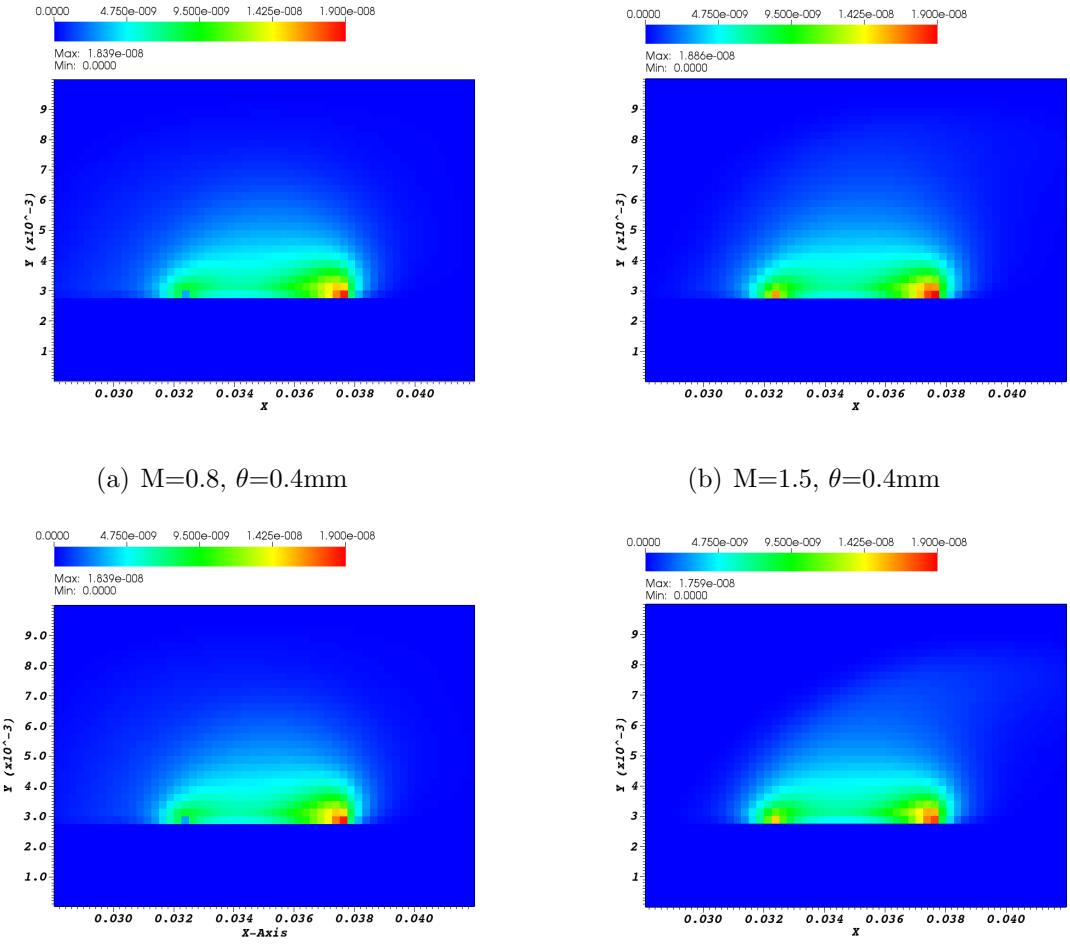

(a) M=0.8, θ=0.4mm

(b) M=1.5, θ=0.4mm

(c) M=0.8, θ=0.1mm

(d) M=3.0, θ=0.4mm

Figure 5.2: Helium ion density distribution under direct discharge [$mol\ m^{-3}$].

and investigate the effects of electron temperature and chemistry on the force and heat sources acting on the flow.

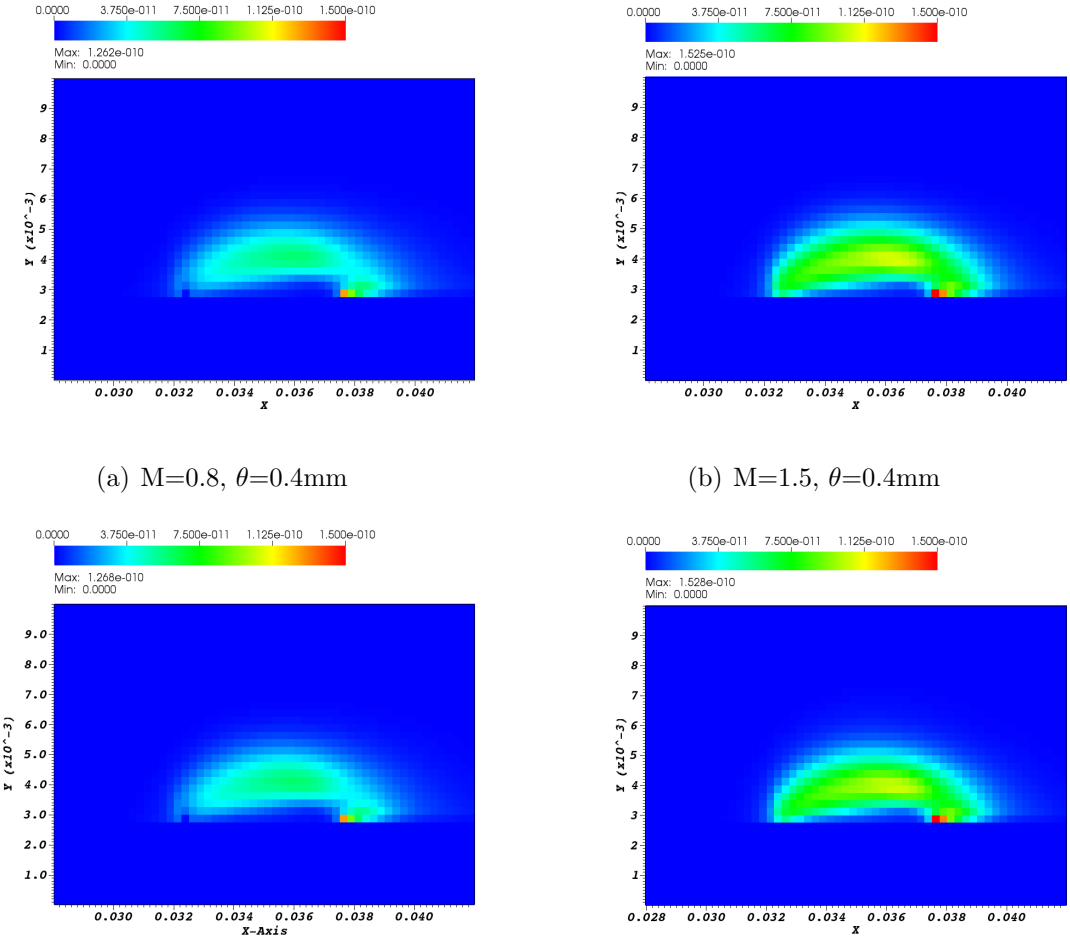

(a) M=0.8, θ=0.4mm

(b) M=1.5, θ=0.4mm

(c) M=0.8, θ=0.1mm

(d) M=3.0, θ=0.4mm

Figure 5.3: Electron density distribution under direct discharge [$mol\ m^{-3}$].

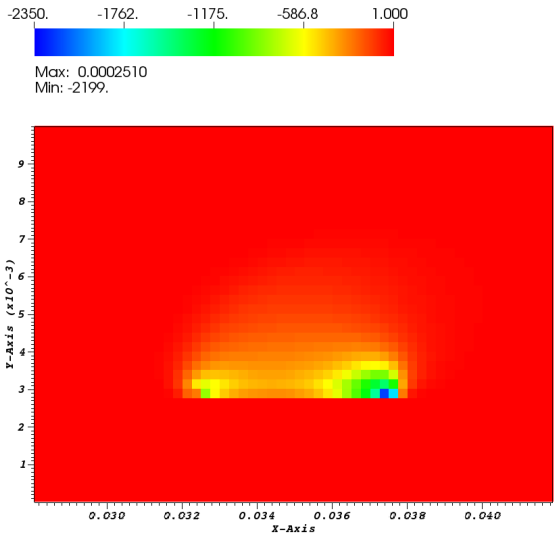

Figure 5.4: Horizontal force density f_x in $[Nm^{-3}]$ under direct discharge with M=0.8 and θ=0.4mm.

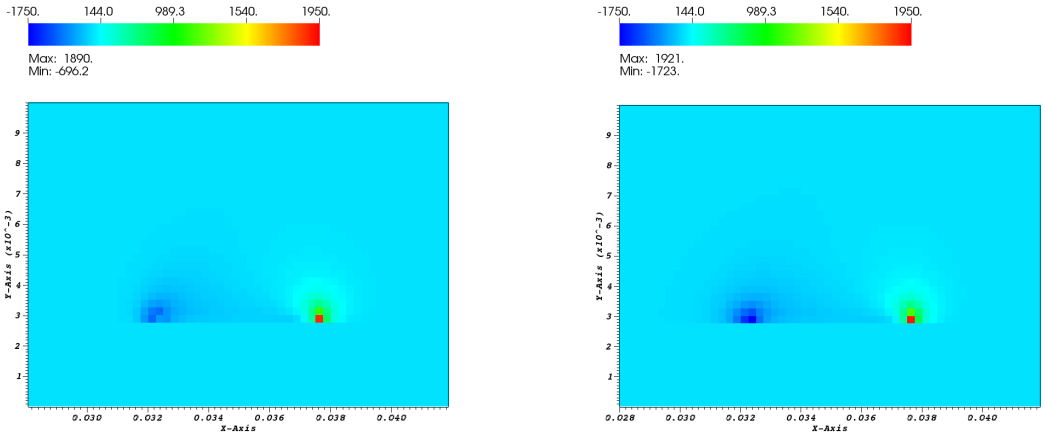

(a) M=0.8, θ=0.4mm

(b) M=1.5, θ=0.4mm

Figure 5.5: Vertical force density f_y in $[Nm^{-3}]$ under direct discharge (the scale is skewed towards the maximum value).

CHAPTER 6

CONCLUSIONS AND FUTURE WORK

The presented work was centered on an investigation of the effects of compressibility and convective velocity on the receptivity of high-speed flows to weakly ionized plasma discharges such as those generated by Dielectric Barrier Discharge actuators.

In the first part of the study, an adjoint formulation of the receptivity problem for compressible quasi-parallel boundary layers was derived. This approach enables the study of mode amplification in response to various external excitations, by means of the eigensolutions of the homogeneous regular and adjoint linearized systems, that need to be computed only once. It was shown that the region of optimum sensitivity to forcing shifts deeper into the flow with increasing Mach number (e.g. by over 50% between M=0.5 and M=1.5), with significantly decreased amplitude, and Reynolds number and frequency dependence resembling that of incompressible flows. Near-wall momentum and heat source two-dimensional profiles representative of DBD forcing were used as excitation, assumed independent of flow conditions, with Mach number in the range of $[0.5, 1.8]$ and Reynolds number up to 2000. The steep amplitude changes of the receptivity coefficients with Mach number and scaling as well as the changes in relative importance between source types under thoses variations underline the importance of receptivity modeling and accordingly tailored actuation design for a successful implementation of DBD devices in supersonic systems.

In order to investigate possible impact of high speed flows on forcing by weakly ionized plasma discharges, a coupled plasma-fluid solver has been built into an adap-

tive mesh refinement framework. It integrates the dielectric layer as part of the solution domain. Mixed Dirichlet-Neumann boundary conditions were implemented for the Poisson solver, with the option to account for the surface charge to adjust the dielectric displacement at the wall. The dielectric displacement boundary condition at the dielectric interface was implemented by stencil manipulation. The implemented gas chemistries include a three-species helium system and an eleven-species air system accounting for non-equilibrium electron energy distribution. The electron-related transport and reaction rate coefficients were extracted as function of the electron temperature from the BOLSIG+ electron Boltzmann transport equation solver.

Preliminary direct discharge simulations were carried out with the new solver using the helium model between $M = 0.8$ and $M = 3.0$, assuming an adiabatic wall and constant electron temperature. Ion convection was observed at the periphery of the glow away from the area of maximum momentum transfer to the flow, whereas the vertical component of the electrohydrodynamic force showed significant difference mostly at the cathode. No large difference in force profile could be observed in the bulk of the discharge, supporting the assumption of a flow-independent forcing taken in Chapter 2 for this particular system.

Electron local heating effects are expected to be significant and will be the subject of next studies under direct discharge and dynamic DBD operation. Next activities will also focus on expanding the program capabilities. Future work includes the replacement of the Poisson solver by a conductivity solver to reduce the system stiffness, implementation of a new implicit solver and more flexible embedded boundary handling. These developments shall support the study of 3D receptivity using realistic chemistry models and multi-actuator geometries, and the study of optimum actuator and actuation design for supersonic flow applications.

REFERENCES

[1] D. Hill, "Adjoint systems and their role in the receptivity problem for boundary layers," *Journal of fluid mechanics*, vol. 292, pp. 183–204, 1995.

[2] D. Marshall, A. Fedorov, and V. Soloviev, "Mathematical fluid dynamics of plasma control over high speed wings," Teledyne Scientific and Imaging Company, Progress report Contract Nr. FA0550-07-C-0039, February 2009.

[3] L. Viehland and E. Mason, "Transport properties of gaseous ions over a wide energy range, iv," *Atomic Data and Nuclear Data Tables*, vol. 60, no. 1, pp. 37–95, 1995.

[4] Y. Itikawa, "Cross sections for electron collisions with nitrogen molecules," *Journal of Physical and Chemical Reference Data*, vol. 35, no. 1, 2006.

[5] ——, "Cross sections for electron collisions with oxygen molecules," *Journal of Physical and Chemical Reference Data*, vol. 38, no. 1, 2009.

[6] Y. Raizer, *Gas Discharge Physics*. Springer Verlag, Berlin, 1997.

[7] M. Lieberman and A. Lichtenbert, *Principles of Plasma Discharges and Materials Processing, 2nd Edition*. Wiley, 2005.

[8] S. Mahadevan, "Simulation of direct-current surface plasma discharges in air for supersonic flow control," Ph.D. dissertation, The University of Texas at Austin, May 2010.

[9] D. Caruana, "Plasmas for aerodynamic control," *Plasma Physics and Controlled Fusion*, vol. 52, p. 124045, 2010.

[10] S. Leonov, I. Kochetov, A. Napartovich, V. Sabel'Nikov, and D. Yarantsev, "Plasma-induced ethylene ignition and flameholding in confined supersonic air

flow at low temperatures," *Plasma Science, IEEE Transactions on*, no. 99, pp. 1–7, 2011.

[11] S. Leonov, A. Firsov, Y. Isaenkov, M. Shurupov, D. Yarantsev, and M. Schneider, "Plasma-based fast mixing and ignition in supersonic flow," in *17th AIAA International Space Planes and Hypersonic Systems and Technologies Conference*, no. AIAA 2011-2327, April 2011.

[12] S. Leonov, A. Firsov, D. Yarantsev, F. Falempin, and A. Miller, "Active steering of shock waves in compression ramps by nonuniform plasma," in *48th AIAA Aerospace Sciences Meeting*, no. AIAA 2010-260, January 2010.

[13] N. Bisek, D. Rizzetta, and J. Poggie, "Exploration of plasma control for supersonic turbulent flow over a compression ramp," in *42nd AIAA Fluid Dynamics Conferences and Exhibit*, no. AIAA 2012-2700, June 2012.

[14] C. Enloe, T. McLaughlin, R. VanDyken, K. Kachner, E. Jumper, and T. Corke, "Mechanisms and responses of a single dielectric barrier plasma actuator: plasma morphology," *AIAA journal*, vol. 42, no. 3, pp. 589–594, 2004.

[15] C. Enloe, T. McLaughlin, R. VanDyken, K. Kachner, E. Jumper, T. Corke, M. Post, and O. Haddad, "Mechanisms and responses of a single dielectric barrier plasma actuator: geometric effects," *AIAA journal*, vol. 42, no. 3, pp. 595–604, 2004.

[16] S. Macheret, "Physics of magnetically accelerated nonequilibrium surface discharges in high-speed flow," in *44th AIAA Aerospace Sciences Meeting and Exhibit*, no. AIAA 2006-1005, January 2006.

[17] E. Moreau, "Airflow control by non-thermal plasma actuators," *Journal of Physics D: Applied Physics*, vol. 40, p. 605, 2007.

[18] T. Corke, M. Post, and D. Orlov, "Sdbd plasma enhanced aerodynamics: concepts, optimization and applications," *Progress in Aerospace Sciences*, vol. 43, no. 7-8, pp. 193–217, 2007.

[19] K. Choi, T. Jukes, and R. Whalley, "Turbulent boundary-layer control with plasma actuators," *Philosophical Transactions of the Royal Society A: Mathematical, Physical and Engineering Sciences*, vol. 369, no. 1940, pp. 1443–1458, 2011.

[20] P. Huang, J. Shang, and S. Stanfield, "Periodic electrodynamic field of dielectric barrier discharge," *AIAA journal*, vol. 49, no. 1, pp. 119–127, 2011.

[21] N. Benard and E. Moreau, "Ehd force and electric wind produced by surface dielectric barrier discharge plasma actuators used for airflow control," in *6th AIAA Flow Control Conference*, no. AIAA 2012-3136, June 2012.

[22] W. Shyy, G. Jayaraman, and A. Andersson, "Modeling of glow discharge induced fluid dynamics," *Journal of Applied Physics*, vol. 92, no. 11, pp. 6434–6443, 2002.

[23] S. Leonov and D. Yarantsev, "Mechanisms of flow control by near-surface electrical discharge generation," in *43rd AIAA Aerospace Sciences Meeting and Exhibit*, no. AIAA-2005-780, January 2005.

[24] S. Roy and C. Wang, "Bulk flow modification with horseshoe and serpentine plasma actuators," *J. Physics D: Applied Physics*, vol. 42, no. 032004, 2009.

[25] B. Gibson, M. Arjomandi, and R. Kelso, "The response of a flat plate boundary layer to an orthogonally arranged dielectric barrier discharge actuator," *J. Physics D: Applied Physics*, vol. 45, no. 025202, 2012.

[26] V. Boucinha, R. Weber, and A. Kourta, "Drag reduction of a 3d bluff body using plasma actuators," *International Journal of Aerodynamics*, vol. 1, no. 3/4, 2011.

[27] L. Osmokrovic, R. Hanson, and P. Lavoie, "Effect of plasma actuator geometry and excitation for producing transient growth modes in a laminar boundary layer," in *6th AIAA Flow Control Conference*, June 2012.

[28] Z. Chen, L. Hao, and B. Zhang, "A model for nano-second pulsed dielectric barrier discharge (nsdbd) actuator and its investigation on the mechanisms of separation control over an airfoil," *Science China, Technological Sciences*, 2013.

[29] W. Saric, "Stability and transition of three-dimensional boundary layers," *Annual Review of Fluid Mechanics*, vol. 35, pp. 413–440, 2003.

[30] C. Schuele, "Control of stationary crossflow modes using passive patterned roughness and dbd plasma actuators at mach 3.5," Ph.D. dissertation, University of Notre Dame, September 2011.

[31] S. Roy and D. Gaitonde, "Force interaction of high pressure glow discharge with fluid flow for active separation control," *Physics of Plasmas*, vol. 13, p. 023503, 2006.

[32] A. Likhanskii, M. Shneider, S. Macheret, and R. Miles, "Modeling of dielectric barrier discharge plasma actuators driven by repetitive nanosecond pulses," *Physics of Plasmas*, vol. 14, p. 073501, 2007.

[33] K. Singh and S. Roy, "Modeling plasma actuators with air chemistry for effective flow control," *Journal of Applied Physics*, vol. 101, p. 123308, 2007.

[34] S. Macheret, M. Shneider, and R. Miles, "Modeling of air plasma generation by repetitive high-voltage nanosecond pulses," *IEEE Transactions on Plasma Science*, vol. 30, no. 3, pp. 1301–1314, June 2002.

[35] V. Soloviev and V. Krivtsov, "Surface barrier discharge modelling for aerodynamic applications," *Journal of Physics D: Applied Physics*, vol. 42, p. 125208, 2009.

[36] A. Likhanskii, "Particle-in-cell modeling of the pulsed dbd plasma actuator," in *40th Fluid Dynamics Conference and Exhibit*, no. AIAA 2010-5101, July 2010.

[37] J. Shin, "A study of direct-current surface discharge plasma for a mach 3 supersonic flow control," Ph.D. dissertation, The University of Texas at Austin, August 2007.

[38] C. Kalra, M. Shneider, and R. Miles, "Numerical study of boundary layer separation control using magnetogasdynamic plasma actuators," *Physics of Fluids*, vol. 21, p. 106101, 2009.

[39] J. Shang, "Surface direct current discharge for hypersonic flow control," no. AIAA 2008-1352, January 2008.

[40] A. Likhanskii, V. Semak, M. Shneider, D. Opaits, R. Miles, and S. Macheret, "Parallel code development and numerical investigation of surface charge build-up in dbd plasma actuators," in *46th AIAA Aerospace Sciences Meeting and Exhibit*, no. AIAA 2008-1380, January 2008.

[41] P. Schmid and D. Henningson, *Stability and transition in shear flows*. Springer Verlag, 2001.

[42] M. Barone and S. Lele, "Receptivity of the compressible mixing layer," *Journal of Fluid Mechanics*, vol. 540, pp. 301–336, 2005.

[43] F. Giannetti and P. Luchini, "Structural sensitivity of the first instability of the cylinder wake," *Journal of Fluid Mechanics*, vol. 581, pp. 167–197, 2007.

[44] M. Barone, "Receptivity of compressible mixing layers," Ph.D. dissertation, Stanford University, 2003.

[45] J. Dongarra, B. Straughan, and D. Walker, "Chebyshev tau-qz algorithm methods for calculating spectra of hydrodynamic stability problems," *Applied Numerical Mathematics*, vol. 22, no. 4, pp. 399–434, 1996.

[46] J. Boeuf and L. Pitschford, "Electrodynamic force and aerodynamic flow acceleration in surface dielectric barrier discharge," *J. Applied Physics*, vol. 97, no. 103307, 2005.

[47] K. Singh, S. Roy, and D. Gaitonde, "Modeling of dielectric barrier discharge plasma actuator with atmospheric air chemistry," in *37th AIAA Plasmadynamics and Lasers Conference*, no. AIAA 2006-3381, San Fransisco, CA, June 2006.

[48] A. Likhanskii, M. Shneider, S. Macheret, and R. Miles, "Optimization of dielectric barrier discharge plasma actuators driven by repetitive nanosecond pulses," in *45th AIAA Aerospace Sciences Meeting and Exhibit*, no. AIAA 2007-633, Reno NV, 2007.

[49] K. Singh and S. Roy, "Force approximation for a plasma actuator operating in atmospheric air," *J. Applied Physics*, vol. 103, no. 013305, 2008.

[50] B. Mertz and T. Corke, "Single-dielectric barrier discharge plasma actuator modelling and validation," *J. Fluild Mechanics*, vol. 669, pp. 557–583, 2011.

[51] G. Font, S. Jung, T. McLaughlin, W. Morgan, and J. Baughn, "Simulation of the effects of force and heat produced by a plasma actuator on neutral flow evolution," in *44th AIAA Aerospace Sciences Meeting and Exhibit*, no. AIAA 2006-167, Reno, NV, January 2006.

[52] G. Font, C. Enloe, and T. McLaughlin, "Plasma volumetric effects on the force production of a plasma actuator," *AIAA Journal*, vol. 48, no. 9, pp. 1869–1874, September 2010.

[53] A. Hoskinson, N. Hcrshkowitzf, and D. Ashpist, "Force measurements of single and double barrier dbd plasma actuators in quiescent air," in *47th Aerospace Sciences Meeting*, no. AIAA 2009-485, Orlando, FL, 2009.

[54] G. Font, C. Enloe, J. Newcomb, A. Teague, A. Vasso, and T. McLaughlin, "Effects of oxygen content on dielectric barrier discharge plasma actuator behavior," *AIAA Journal*, vol. 49, no. 7, pp. 1366–1373, July 2011.

[55] A. Likhanskii, M. Shneider, S. Macheret, and R. Miles, "Modeling of interaction between weakly ionized near-surface plasmas and gas flow," in *44th AIAA Aerospace Sciences Meeting and Exhibit*, no. AIAA 2006-1204. AIAA, January 2006.

[56] D. Marshall, A. Fedorov, and V. Soloviev, "Mathematical fluid dynamics of plasma control over high speed wings," Teledyne Scientific and Imaging Company, Tech. Rep. FA9550-09-C-0213, December 2010.

[57] M. Denison and L. Massa, "On gasdynamic instabilities supported by non-equilibrium plasma in a supersonic flow," in *6th AIAA Flow Control Conference*, no. AIAA-2012-2737, June 2012.

[58] G. Hagelaar, "Modeling of microdischarges for display technology," Ph.D. dissertation, Technische Universiteit Eindhoven, 2000.

[59] S. Jardin, *Computational methods in plasma physics*. CRC Press, 2010.

[60] R. Kee, G. Dixon-Lewis, J. Warnatz, M. Coltrin, and J. Miller, "A fortran computer code package for the evaluation of gas-phase multi-component transport properties," Sandia Labs, Tech. Rep. SAND86-8246, 1986.

[61] Y. Sakiyama and D. Graves, "Nonthermal atmospheric rf plasma in one-dimensional spherical coordinates: asymmetric sheath structure and the discharge mechanism," *Journal of Applied Physics*, vol. 101, p. 073306, 2007.

[62] T. Deconinck, S. Mahadevan, and L. Raja, "Discretization of the joule heating term for plasma discharge fluid models in unstructured meshes," *Jornal of Computational Physics*, vol. 228, pp. 4435–4443, 2009.

[63] G. Hagelaar, F. de Hoog, and G. Kroesen, "Boundary conditions in fluid models of gas discharges," *Physical Review E*, vol. 62, no. 1, pp. 1452–1454, 2000.

[64] W. Criminale, T. Jackson, and R. Joslin, *Theory and computation in hydrodynamic stability*. Cambridge University Press, UK., 2003.

[65] H. Ellis, R. PAI, and E. McDaniel, "Transport properties of gaseous ions over a wide energy range," *Atomic Data and Nuclear Data Tables*, vol. 17, pp. 177–210, 1976.

[66] I. Kossyi, A. Kostinsky, A. Matveyev, and V. Silakov, "Kinetic scheme of the non-equilibrium discharge in nitrogen-oxygen mixtures," *Plasma Sources Science and Technology*, vol. 1, pp. 207–220, 1992.

[67] G. Hagelaar and L. Pitchford, "Solving the boltzmann equation to obtain electron transport coefficients and rate coefficients for fluid models," *Plasma Sources Science and Technology*, vol. 14, pp. 722–733, 2005.

[68] D. Nelson, M. Benhenni, O. Eichwald, and M. Yousfi, "Ion swarm data for electrical discharge modeling in air and flue gas mixtures," *Journal of Applied Physics*, vol. 94, no. 1, pp. 96–103, 2003.

[69] A. Bekstein, M. Benhenni, M. Yousfi, O. Ducasse, and O. Eichwald, "Ion swarm data of n4+ in n2, o2 and dry air for streamer dynamics simulation," *European Physical Journal. Applied Physics: EPJ.*, vol. 42, no. 1, 2008.

[70] R. van Sonsbeek, R. Cooper, and R. Bhave, "Pulse radiolysis studies of ion-electron recombination in helium. pressure and temperature effects," *J. Chem. Phys.*, vol. 97, no. 3, pp. 1800–1808, 1992.

[71] P. Colella, D. Graves, B. Keen, and D. Modiano, "A cartesian grid embedded boundary method for hyperbolic conservation laws," *Journal of Computational Physics*, vol. 211, pp. 347–366, 2006.

[72] P. Ravindran, "Investigation of instabilities affecting detonations: Improving the resolution using block-structured adaptive mesh refinement," Ph.D. dissertation, University of Texas at Arlington, May 2012.

BIOGRAPHICAL STATEMENT

Marie Denison was born in Huy, Belgium in 1974. She received her M.S. degree in Applied Physics from the University of Liege, Belgium in 1997 and Ph.D. in Electrical Engineering from the University of Bremen, Germany in 2005. From 1998 to 2005, she worked at Infineon Technologies, Munich, Germany on the development and modeling of smart power integrated circuit technologies for the automotive industry. In 2005, she joined Texas Instruments, Dallas, TX, where she developed various analog semiconductor technologies, power components and packaging solutions for consumer, automotive and offline markets, while fostering various research programs in these areas. She is interested in computational multi-physics modeling, actuator design and high-speed flow control. Marie is a senior member of the IEEE and a member of the AIAA.